Monthly Notices of the ROYAL ASTRONOMICAL SOCIETY

MNRAS **531,** 1256–1275 (2024) https://doi.org/10.1093/mnras/stae927
Advance Access publication 2024 April 3

Transient fading X-ray emission detected during the optical rise of a tidal disruption event

A. Malyali [1★] A. Rau,[1] C. Bonnerot,[2] A. J. Goodwin,[3] Z. Liu,[1] G. E. Anderson [3] J. Brink,[4,5] D. A. H. Buckley [4,5,6] A. Merloni,[1] J. C. A. Miller-Jones [3] I. Grotova[1] and A. Kawka [3]

[1]*Max-Planck-Institut für extraterrestrische Physik, Giessenbachstrasse 1, 85748 Garching, Germany*
[2]*School of Physics and Astronomy & Institute for Gravitational Wave Astronomy, University of Birmingham, Birmingham B15 2TT, UK*
[3]*International Centre for Radio Astronomy Research, Curtin University, GPO Box U1987, Perth, WA 6845, Australia*
[4]*South African Astronomical Observatory, PO Box 9, Observatory Rd, 7935 Observatory, Cape Town, South Africa*
[5]*Department of Astronomy, University of Cape Town, Private Bag X3, Rondebosch 7701, South Africa*
[6]*Department of Physics, University of the Free State, PO Box 339, Bloemfontein 9300, South Africa*

Accepted 2024 March 27. Received 2024 March 2; in original form 2023 August 2

ABSTRACT

We report on the *SRG*/eROSITA detection of ultra-soft ($kT = 47^{+5}_{-5}$ eV) X-ray emission ($L_X = 2.5^{+0.6}_{-0.5} \times 10^{43}$ erg s^{-1}) from the tidal disruption event (TDE) candidate AT 2022dsb ∼14 d before peak optical brightness. As the optical luminosity increases after the eROSITA detection, then the 0.2–2 keV observed flux decays, decreasing by a factor of ∼39 over the 19 d after the initial X-ray detection. Multi-epoch optical spectroscopic follow-up observations reveal transient broad Balmer emission lines and a broad He II 4686 Å emission complex with respect to the pre-outburst spectrum. Despite the early drop in the observed X-ray flux, the He II 4686 Å complex is still detected for ∼40 d after the optical peak, suggesting the persistence of an obscured hard ionizing source in the system. Three outflow signatures are also detected at early times: (i) blueshifted H α emission lines in a pre-peak optical spectrum, (ii) transient radio emission, and (iii) blueshifted Ly α absorption lines. The joint evolution of this early-time X-ray emission, the He II 4686 Å complex, and these outflow signatures suggests that the X-ray emitting disc (formed promptly in this TDE) is still present after optical peak, but may have been enshrouded by optically thick debris, leading to the X-ray faintness in the months after the disruption. If the observed early-time properties in this TDE are not unique to this system, then other TDEs may also be X-ray bright at early times and become X-ray faint upon being veiled by debris launched shortly after the onset of circularization.

Key words: accretion, accretion discs – black hole physics – galaxies: nuclei – transients: tidal disruption events.

1 INTRODUCTION

The number of stellar tidal disruption event (TDE) candidates identified in recent years has greatly increased, largely fuelled by the increasing number of wide-field high-cadence time-domain surveys operating across the electromagnetic spectrum. Although early theoretical work predicted TDEs to produce large amplitude ultra-soft X-ray flares originating from the centres of galaxies (Rees 1988) – consistent with the first TDE candidates identified by *ROSAT* (Trümper 1982) in the 1990s (Bade, Komossa & Dahlem 1996; Grupe, Thomas & Leighly 1999; Komossa & Bade 1999; Komossa & Greiner 1999; Greiner et al. 2000) – the majority of optically selected TDE candidates do not show transient X-ray emission (van Velzen et al. 2021; Hammerstein et al. 2023). To explain the dearth of X-rays in these systems, it has been suggested that the optical emission is produced by the debris circularization process instead of accretion (stream-stream collisions; Piran et al. 2015; Shiokawa et al. 2015), or that a large fraction of the X-ray emission is reprocessed to optical/UV bands by debris enveloping the nascent disc (Loeb & Ulmer 1997; Lodato & Rossi 2011; Miller 2015; Metzger & Stone 2016; Dai et al. 2018; Lu & Bonnerot 2020).

Optical spectroscopic follow-up of optically bright TDEs has led to the classifications of TDEs into different spectral types (e.g. Arcavi et al. 2014; Leloudas et al. 2019; Velzen et al. 2021), depending on the emission lines seen in the spectra. These are (i) 'H', which show transient broad Balmer emission lines, (ii) 'H + He', showing transient broad Balmer emission lines and a broad emission complex around He II 4686 A, and (iii) 'He', which show a transient broad He II 4686 A emission feature but no Balmer emission. An additional spectral TDE class not common in recent optically selected TDE samples are the extreme coronal line emitters (ECLEs; Komossa et al. 2009; Wang et al. 2011, 2012), which show strong emission from high-ionization coronal lines with respect to their narrow [O III] 5007 Å emission. A hard ionizing source (photons with energy above 54 eV) is needed to produce the He II emission seen in 'He' and 'H + He' TDEs (herein collectively referred to as He-TDEs), yet the majority of TDE candidates even in these classes do not show transient X-ray emission (Hammerstein et al. 2023). As it is thought that these hard photons originate from the high-energy tail of the

★ E-mail: amalyali@mpe.mpg.de

newly formed disc, then the combination of the X-ray faintness and the He II emission in these systems has been suggested as evidence for 'obscured accretion' (Leloudas et al. 2019), where an accretion disc has formed in these systems, but its high-energy emission gets reprocessed into the optical band by an optically thick gaseous envelope. Several TDE candidates have also shown broad He II lines close to peak optical brightness (Blagorodnova et al. 2017; Nicholl et al. 2020; Wevers et al. 2022), which under the assumption of an obscured accretion-driven origin, suggests efficient circularization of the debris into a disc post-disruption.

Here, we report on multiwavelength observations of the TDE candidate AT 2022dsb, which shows a factor of 39 decrease in its 0.2–2 keV observed flux during the optical rise. Section 2 describes the discovery of AT 2022dsb, whilst Sections 3 and 4 detail multiwavelength observations of the system and their analysis, respectively. In Section 5, we review previous X-ray observations of TDEs at early times and compare these with AT 2022dsb. The implications of our observational campaign are discussed in Section 6, and our conclusions in Section 7. All magnitudes are reported in the AB system and corrected for Galactic extinction using $A_V = 0.62$ mag, obtained from Schlafly & Finkbeiner (2011), $R_V = 3.1$ and a Cardelli extinction law (Cardelli, Clayton & Mathis 1989). The effective wavelength for each filter was retrieved from the SVO Filter Profile Service.[1] All dates and times will be reported in universal time (UT).

2 DISCOVERY

AT 2022dsb/ eRASSt J154221.6−224012 was independently discovered by the extended ROentgen Survey with an Imaging Telescope Array (eROSITA; Predehl et al. 2021), the soft X-ray instrument on board the *Spektrum–Roentgen–Gamma* (SRG; Sunyaev et al. 2021) observatory, during a systematic search for TDE candidates in the fifth eROSITA All-Sky Survey (eRASS5), when it was observed on 2022-02-17 as a new, bright (0.2–2 keV observed flux of $\sim 3 \times 10^{-13}$ erg cm^{-2} s^{-1}), ultra-soft (Section 4.1) X-ray point source. Using the *eROSITA Science Analysis Software* pipeline (ESASS;[2] Brunner et al. 2022), the source was localized to (RA_{J2000}, $Dec._{J2000}$) = (15h42m21.6s,−22°40′12.1″), with a 1σ positional uncertainty of 1.9 arcsec (68 per cent confidence), consistent with the galaxy ESO 583-G004 at $z = 0.0235$ (Fig. 1). No X-ray source had been detected within 30 arcsecof this position in any of the previous four eRASS, with a 3σ upper limit on the 0.2–2 keV band flux of 5×10^{-14} erg cm^{-2} s^{-1}, assuming the same spectral model fitted to the eRASS5 spectrum (Liu et al. 2022). The last non-detection by eROSITA occurred ∼6 months before the eRASS5 detection.

AT 2022dsb was later publicly classified on 2022-03-02 as a TDE candidate in the TNS report TNSCR-2022-584 (Fulton et al. 2022), after the discovery and reporting of optical transient emission (associated to the nucleus of the host galaxy ESO 583-G004) initially by ASAS-SN on 2022-03-01 in Stanek & Kochanek (2022), and then by both the Asteroid Terrestrial Impact Last Alert System (ATLAS; Tonry et al. 2018), and the Zwicky Transient Facility (ZTF; Bellm et al. 2019; Graham et al. 2019) by the ALeRCE alert broker (Förster et al. 2021).

2.1 Host galaxy

A pre-outburst optical spectrum of ESO 583-G004 was taken in 2002 during the Six-Degree Field (6dF; Jones et al. 2009) galaxy survey. A recent analysis of the narrow emission lines in this optical spectrum classified the system as a type II AGN (Chen et al. 2022), according to the criteria presented in Kewley et al. (2001). However, the pre-outburst *AllWISE* (Wright et al. 2010; Mainzer et al. 2014) colour of the host, $W1 - W2 = 0.00 \pm 0.03$ mag, suggests that its mid-infrared emission is dominated by the galaxy light, instead of the luminous emission from a dusty torus surrounding an AGN (Stern et al. 2012; Assef et al. 2018). ESO 583-G004 may have hosted a low-luminosity AGN prior to the outburst of AT 2022dsb, similar to other TDE candidates (e.g. ASASSN-14li; Holoien et al. 2016; AT 2019qiz; Nicholl et al. 2020).

We fitted the DESI Legacy DR10 (Dey et al. 2019) archival photometry of the host galaxy (g, i, $W1$, $W2$, $W3$, and $W4$ bands[3]) with the stellar population inference tool PROSPECTOR (Johnson et al. 2021), which uses a PYTHON wrapper (Foreman-Mackey, Sick & Johnson 2014) of the Flexible Stellar Population Synthesis code (Conroy & Gunn 2010) for generating the SEDs of stellar populations. The SED model includes both stellar and nebular emission, as well as dust attenuation and emission, and adopts a Chabrier initial mass function (IMF; Chabrier 2003); the free parameters are the total stellar mass of the galaxy ($M_{\star,\,\rm gal}$, the sum of both living and remnant stars), the metallicity ($\log(Z/Z_\odot)$), the age of the galaxy ($t_{\rm age}$), the decay timescale under an exponentially declining star formation model ($\tau_{\rm SF}$), and the host galaxy dust extinction (A_V). Posterior distributions were sampled using the dynamic nested sampler (Skilling 2004, 2006; Higson et al. 2019) DYNESTY (Speagle 2020; Koposov et al. 2023), with the posterior model shown in Fig. 2 and the parameter estimates in Table 1. From the inferred $M_{\star,\rm gal} = 7^{+4}_{-3} \times 10^{10}\,M_\odot$ and using the relation between $M_{\rm BH}$ and $M_{\star,\,\rm gal}$ in Reines & Volonteri (2015), we infer $\log[M_{\rm BH}/M_\odot] = 7.3^{+0.2}_{-0.3}$.

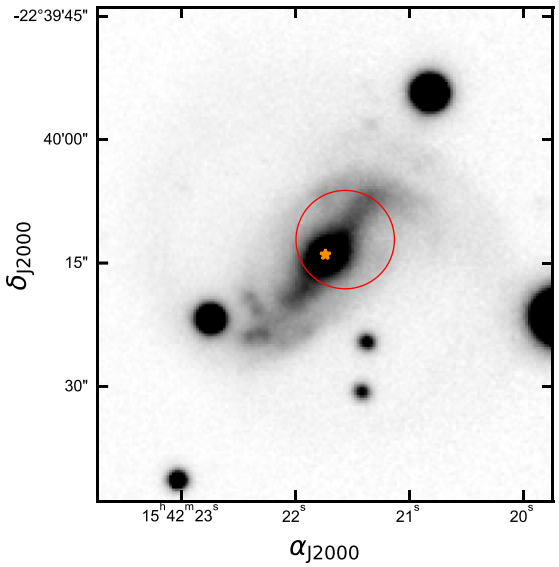

Figure 1. Finder chart for AT 2022dsb (DESI LS DR10 g-band image). The red circle denotes the 3σ uncertainty on the eROSITA source position in eRASS5, whilst the dark orange star marks the *Gaia* DR3 optical centre of the host galaxy ESO 583-G004.

[1] http://svo2.cab.inta-csic.es/theory/fps/
[2] Version: eSASSusers_211214.
[3] No z-band photometry was available for the host of AT 2022dsb in DR10, and all DR10 photometry was taken before August 2021.

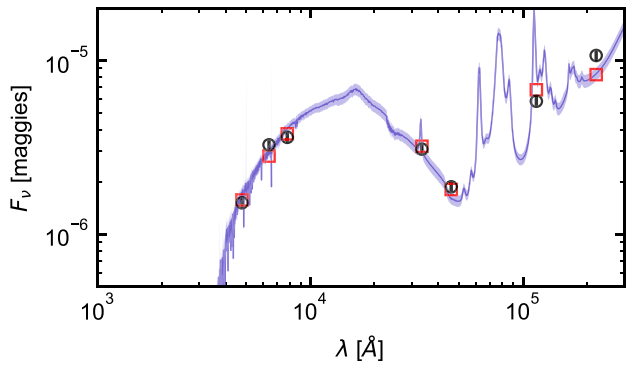

Figure 2. SED fit to the LS DR10 photometry of the host galaxy of AT 2022dsb. The observed photometry is plotted with black edged circular markers, whilst the posterior model and model photometry is shown in blue (solid line represents the median, shaded region encloses the middle 90 per cent of the posterior) and red, respectively.

Table 1. Host galaxy properties inferred via SED fitting to the archival photometry, with CR denoting the credible region for a parameter.

Parameter	68% CR
$M_{\star,\,\mathrm{gal}}/10^{10}\,\mathrm{M}_\odot$	$6.9^{+3.9}_{-3.3}$
$\log\,[Z/Z_\odot]$	$-0.7^{+0.3}_{-0.3}$
A_V/mag	$0.62^{+0.05}_{-0.06}$
t_{age}/Gyr	$5.4^{+4.3}_{-3.2}$
τ_{SF}/Gyr	$0.2^{+0.5}_{-0.1}$

3 OBSERVATIONS AND DATA REDUCTION

After the initial eROSITA discovery, additional X-ray observations of AT 2022dsb were obtained with *XMM–Newton* (Section 3.1.2) and *Swift* XRT (Section 3.1.3); collectively, these sample the X-ray emission from a TDE pre-peak, near-peak, and post-peak optical brightness. The optical, UV, and radio evolution was also monitored with ground-based photometry (Section 3.2.1), *Swift* UVOT (Section 3.2.2), and the Australia Telescope Compact Array (ATCA; Section 3.4), respectively. The full multiwavelength light curve of AT 2022dsb is depicted in Fig. 3, and a comparison of the optical light curve with other TDE candidates is shown in Fig. 4. A log of all X-ray observations and the inferred fluxes is presented in Table 2, whilst the optical and UV photometry can be found in Table A1.

3.1 X-ray

3.1.1 eROSITA

The position of AT 2022dsb was observed by eROSITA during the first four eRASS, (denoted eRASS1, eRASS2, eRASS3, and eRASS4, respectively) on 2020-02-27, 2020-08-26, 2021-02-11, and 2021-08-20. During eRASS5, eROSITA first observed AT 2022dsb on 2022-02-17, scanning over its position seven times over the following day, with each visit separated by four hours (Fig. 5). Using the ESASS task SRCTOOL, we generated source and background spectra by extracting counts from a source aperture of radius 30 arcsec, and a background annulus of inner and outer radii 90 and 240 arcsec, respectively, with both apertures centred on the eROSITA position of AT 2022dsb. The same source and background apertures were used to generate a 0.2–2 keV light curve using SRCTOOL, shown in Fig. 5. AT 2022dsb is clearly detected above background by eROSITA in each of the seven observations within eRASS5 (i.e. is persistently bright, instead of showing a 'one-off' short flaring), providing a lower limit of 1 d on the duration of X-ray emission at early-times in AT 2022dsb. A log of X-ray observations is presented in Table 2.

3.1.2 XMM–Newton

Additional observations of AT 2022dsb were performed with *XMM* (P.I. Z. Liu), with the first taking place ∼19 d after the eRASS5 detection on 2022-03-08, and then ∼173 d after this on 2022-08-29; observations were carried out in imaging mode with the medium filter. To reduce and analyse the *XMM* data, we used HEASOFT (version 6.29), the *XMM* Science Analysis Software (SAS) (version 20211130_0941), and the latest calibration data files. Calibrated event files were generated from the Observation Data Files (ODF) using `emproc` and `epproc` for the MOS and PN cameras, respectively, and periods of high particle background during each observation were filtered out following the *XMM* Science Operation Centre recommended procedures. This resulted in 18.0 ks and 13.3 ks exposures for the first and second observations, respectively. Source spectra were extracted from a circle of radius 20 arcsec, centred on the *Gaia* EDR3 (Gaia Collaboration 2021) position of ESO 583-G004, whilst background spectra were extracted from an annulus with inner and outer radii 76 and 144 arcsec, respectively. Only events with `PATTERN<=4` and `FLAG==0` were extracted for PN, whilst `PATTERN<=12` was applied for MOS1 and MOS2.

3.1.3 Swift XRT

AT 2022dsb was further monitored in the 0.3–10 keV band with the XRT instrument (Burrows et al. 2005) on-board the *Neil Gehrels Swift* observatory (Gehrels et al. 2004).[4] XRT observations commenced on 2022-03-05, ∼16 d after the eRASS5 observation, and were performed in photon counting mode. These were then analysed with the online XRT product building tool provided by the UK Swift Science Data Centre's (UKSSDC) (Evans et al. 2007, 2009). AT 2022dsb was not detected in any of the XRT observations, with 3σ upper limits on the 0.3–2 keV count rates computed using the method presented in Kraft, Burrows & Nousek (1991). These were then converted to 0.2–2 keV fluxes using webPIMMs,[5] where we adopted the spectral model inferred from our BXA fit to the eRASS5 spectrum.

3.2 Photometry

3.2.1 Ground-based photometry

We obtained ATLAS *o* and *c* band (Tonry et al. 2018) light curves of AT 2022dsb using the online forced photometry server (Smith et al. 2020; Shingles et al. 2021). For late-time observations (MJD $>$ 59 635), we performed a weighted rebin of the light curve into 1 d intervals. To improve the sampling of the light curve around peak optical brightness, then no such rebinning was performed for observations performed during the optical rise and the early part of the decay (59 620 $<$ MJD $<$ 59 635). To remove epochs of low quality photometry in the ATLAS light curve, we discarded data points where the semi-major axis of the fitted PSF model was greater than 3 pixels (1.86 arcsec per pixel).

[4]P.I. for *Swift* observations: A. Malyali, P. Charalampopoulos, J. Hinkle, I. Lypova.
[5]https://heasarc.gsfc.nasa.gov/cgi-bin/Tools/w3pimms/w3pimms.pl

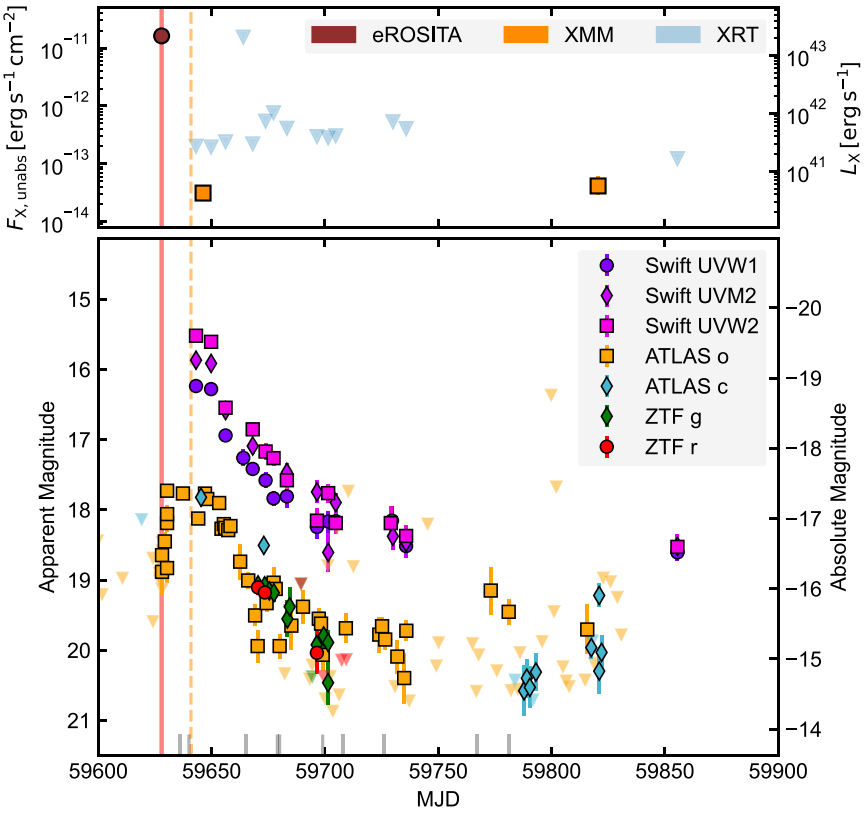

Figure 3. 0.2–2 keV X-ray (top) and optical-UV (bottom) evolution of AT 2022dsb. Solid markers denote $>3\sigma$ detections in each epoch, whereas translucent triangles mark 3σ upper limits. The vertical red line marks the eROSITA observation of AT 2022dsb, whilst the vertical orange line marks the inferred time of optical peak on MJD 59 641 (Section 4.2), ∼14 d after the eRASS5 detection.

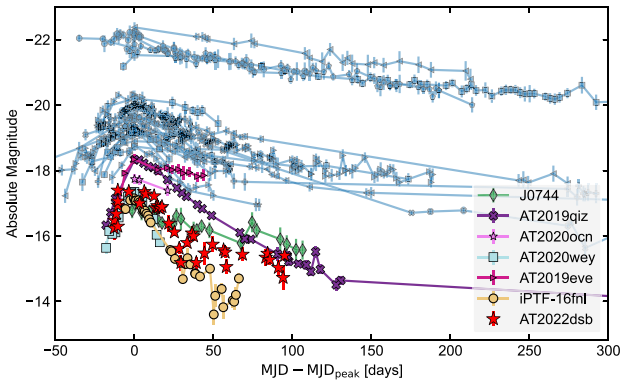

Figure 4. Comparison of the ATLAS *o*-band lightcurve of AT 2022dsb (red stars) with the *g*-band light curves of ZTF-selected TDEs (blue markers) reported in Hammerstein et al. (2023). TDEs of similar peak absolute magnitudes are highlighted in non-dark blue colours, and we include data from the 'faint and fast' TDE iPTF-16fnl (Blagorodnova et al. 2017), and the 'faint and slow' TDE eRASSt J074426.3+291606 (the faintest optically bright TDE observed to date, J0744; Malyali et al. 2023b).

In addition, *g* and *r*-band light curves[6] were generated using the ZTF forced photometry service (Masci et al. 2019), which were then calibrated using the method developed by Miller et al. (in preparation) for the ZTF Bright Transient Survey. [7] No significant optical variability is seen in the ZTF light curves before the 2022 outburst, and we note that the ZTF observations do not sample the rise and peak optical brightness (Fig. 3).

3.2.2 Swift *UVOT*

Over the course of the *Swift* monitoring campaign, AT 2022dsb was observed by the UVOT (Roming et al. 2005) instrument across all filters (*V*, *B*, *U*, *UVW*1, *UVM*2, and *UVW*2), although the number of filters used varied between each observation (see photometry in Table A1). In this work, we use observations performed only in the *UVW*1, *UVM*2, and *UVW*2 filters, since the light curve sampling is highest in these bands, and the optical coverage is already provided by ATLAS and ZTF. We first downloaded the level 2 UVOT sky images from the UK Swift Science Data Centre, before computing aperture photometry on these with the `uvotsource` task (HEASOFT v6.29, CALDB v20201215), using a 5 arcsec radius source aperture, and a nearby, source-free circular aperture of of radius 15 arcsec for the background. Lastly, the recommended Small Scale Sensitivity check[8] was completed.

3.3 Optical spectroscopy

The first follow-up optical spectrum of AT 2022dsb was obtained on 2022-02-26 (MJD = 59 636, ∼5 d before optical peak), using the

[6]This is generated from science images that have already been reference image subtracted

[7]https://github.com/BrightTransientSurvey/ztf_forced_phot
[8]https://swift.gsfc.nasa.gov/analysis/uvot_digest/sss_check.html

Table 2. X-ray light curve of AT 2022dsb. $F_{0.2-2\,\mathrm{keV,\,obs}}$ and $F_{0.2-2\,\mathrm{keV,\,unabs}}$ are the observed (not corrected for Galactic absorption) and unabsorbed 0.2–2 keV band fluxes in units of erg cm^{-2} s^{-1}. log $[L_{0.2-2\,\mathrm{keV}}]$ is inferred from $F_{0.2-2\,\mathrm{keV,\,unabs}}$. MJD is computed from the midpoint of $\mathrm{MJD_{start}}$ and $\mathrm{MJD_{stop}}$. The fluxes have been estimated from the best-fitting model (Table 4), with the 3σ upper limits on the count rates converted to fluxes using the best-fitting model to the eRASS5 spectrum.

MJD	$\mathrm{MJD_{start}}$	$\mathrm{MJD_{stop}}$	Instrument	ObsID	log $[F_{0.2-2\,\mathrm{keV,\,obs}}]$	log $[F_{0.2-2\,\mathrm{keV,\,unabs}}]$	log $[L_{0.2-2\,\mathrm{keV}}]$
59 627.939	59 627.439	59 628.439	eROSITA	eRASS5	$-12.46^{+0.07}_{-0.08}$	$-10.79^{+0.10}_{-0.14}$	$43.34^{+0.10}_{-0.14}$
59 643.115	59 643.004	59643.226	XRT	00 015 054 002	<-12.69	<-11.11	<43.02
59 646.226	59 646.088	59 646.363	EPIC PN	XMM1	$-14.05^{+0.05}_{-0.06}$	$-13.50^{+0.10}_{-0.10}$	$40.62^{+0.10}_{-0.10}$
59 649.772	59 649.702	59 649.842	XRT	00 015 054 003	<-12.71	<-11.12	<43.01
59 656.156	59 656.150	59 656.161	XRT	00 015 054 005	<-12.62	<-11.03	<43.10
59 663.969	59 663.968	59 663.969	XRT	00 015 054 006	<-10.81	<-9.22	<44.90
59 668.128	59 668.030	59 668.225	XRT	00 015 054 007	<-12.65	<-11.07	<43.06
59 673.808	59 673.805	59 673.811	XRT	00 015 054 008	<-12.26	<-10.67	<43.45
59 677.316	59 677.178	59 677.453	XRT	00 015 054 009	<-12.12	<-10.53	<43.60
59 683.209	59 683.205	59 683.214	XRT	00 015 054 010	<-12.38	<-10.80	<43.33
59 696.480	59 696.206	59 696.755	XRT	00 015 054 011	<-12.53	<-10.94	<43.19
59 701.425	59 701.251	59 701.598	XRT	00 015 054 012	<-12.55	<-10.96	<43.16
59 704.749	59 704.513	59 704.986	XRT	00 015 054 013	<-12.51	<-10.93	<43.20
59 729.976	59 729.051	59 730.902	XRT	00 015 054 014	<-12.27	<-10.68	<43.44
59 735.808	59 735.801	59 735.816	XRT	00 015 054 015	<-12.39	<-10.80	<43.32
59 820.520	59 820.376	59 820.664	EPIC PN	XMM2	$-14.18^{+0.08}_{-0.08}$	$-13.38^{+0.16}_{-0.15}$	$40.75^{+0.16}_{-0.15}$
59 855.517	59 855.146	59 855.888	XRT	00 015 054 016	<-12.91	<-11.32	<42.81

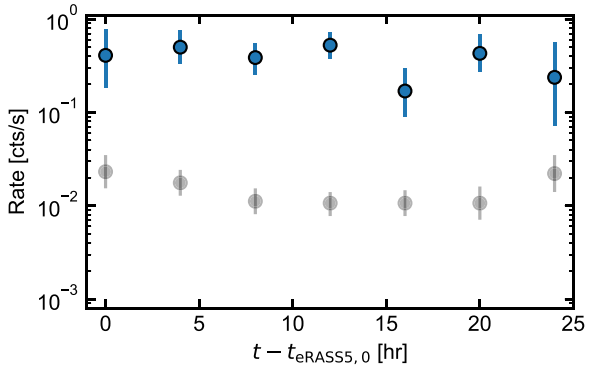

Figure 5. eRASS5 light curve of AT 2022dsb in the 0.2–2 keV band. The blue markers denote the source count rates (corrected for vignetting), whilst the grey markers show the estimated background count rates. $t - t_{\mathrm{eRASS5,\,0}}$ is the time relative to the start of eROSITA's observations of AT 2022dsb in eRASS5 (MJD = 59 627.439). AT 2022dsb is persistently bright over the day-long monitoring window in eRASS5.

FLOYDS spectrograph mounted on the 2m Las Cumbres Observatory (LCO; Brown et al. 2013)[9] telescope at Haleakala Observatory. Data processing and spectrum extraction were performed by the automatic FLOYDS pipeline at LCO (further details on the spectroscopic data reduction are presented in Section B). This spectrum (Fig. 6) shows transient broad Balmer emission lines (Hα, Hβ), a broad emission complex around 4600 Å, and a blue continuum, with the transient nature confirmed through comparison to archival and late-time optical spectra. In addition, narrow emission lines (Hα, Hβ, [N II] 6548 and 6583 Å, and the high-ionization lines [O III] 4959 and 5007 Å), as well as several host galaxy absorption features, are clearly present. No strong blue continuum or broad emission lines were seen in a pre-outburst optical spectrum taken on 2002-04-15

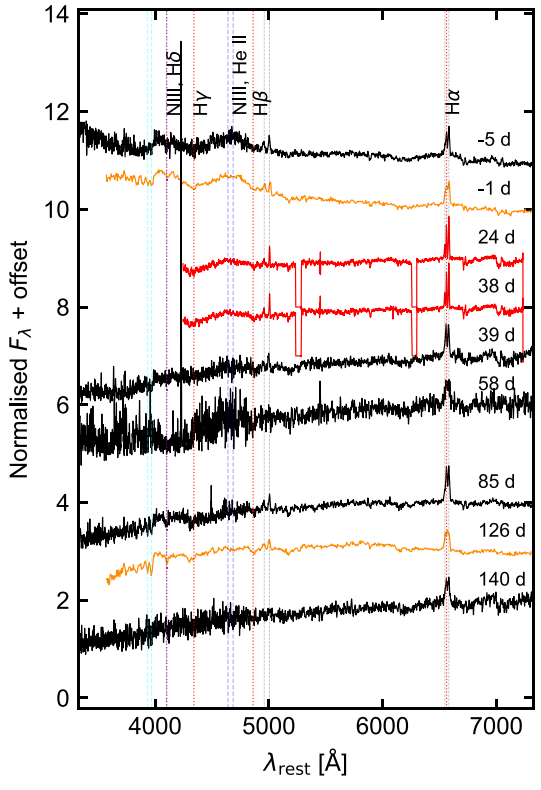

Figure 6. Optical spectroscopic evolution of AT 2022dsb. The phase of the observation with respect to the inferred optical peak (MJD = $59640.9^{+0.5}_{-0.4}$) is shown on the right hand side above each spectrum. Black, orange, and red spectra were obtained using LCO/FLOYDS, NTT/EFOSC2, and SALT/RSS, respectively. The archival spectrum of the host galaxy is presented in Fig. B2.

[9]Proposal ID CON2022A-001, PI: M. Salvato.

Table 3. ATCA radio observations of AT 2022dsb.

MJD	Date	Array config.	Frequency (GHz)	Flux density (μJy)
59 661	2022-03-23	6A	5.5	593 ± 19
59 661	2022-03-23	6A	9	536 ± 17
59 819	2022-08-28	6D	5.5	211 ± 11
59 819	2022-08-28	6D	9	152 ± 10
59 912	2022-11-29	6C	5.5	171 ± 8
59 912	2022-11-29	6C	9	127 ± 6

during the 6dF Galaxy Survey (6dFGS; Jones et al. 2009). Over the 140 d of spectroscopic monitoring of AT 2022dsb after optical peak, the strength of the broad emission lines and the blue continuum relative to the host galaxy decreases (Fig. 6). Zoom-in plots on the evolution of the H α and He II complexes are presented in Fig. B1.

3.4 Radio

3.4.1 Archival

The Karl G. Jansky Very Large Array Sky Survey (VLASS; Lacy et al. 2020) observed the coordinates of AT2022dsb on 2020-11-03 and 2018-02-15, approximately 1 and 4 yr prior to the detection of the transient event. There is no source present at the location of AT2022dsb in either of these observations, with a 3σ upper limit of 507 and 419 μJy at 3 GHz for the 2020 and 2018 observations, respectively.

3.4.2 Follow-up

We observed the coordinates of AT2022dsb on three occasions with the Australia Telescope Compact Array (ATCA) between 2022 March and November (project C3334, PI Anderson/Goodwin). Observations were taken in the 4-cm band with the dual 5.5 and 9 GHz receiver. Further, more detailed radio spectral monitoring of AT2022dsb is being carried out and will be published in a follow-up paper (Goodwin et al. in preparation). Because of the early eROSITA detection of AT 2022dsb, then the ATCA observations presented here represent one of the earliest radio detections of a TDE.

The ATCA data were reduced using the Common Astronomy Software Application (CASA v 5.6.3; The CASA Team et al. 2022) using standard procedures including flux and bandpass calibration with PKS 1934−638 and phase calibration with PKS 1514−241. The target field was imaged using the CASA task `tclean` with an image size of 4000 pixels and a cellsize of 0.3 arcsec at 5.5 GHz and an image size of 4000 pixels and a cellsize of 0.2 arcsec at 9 GHz. In all observations, a point source was detected at the location of AT2022dsb. The flux density of the point source was extracted in the image plane using the CASA task `imfit` by fitting an elliptical Gaussian fixed to the size of the synthesized beam. A summary of the ATCA observations is given in Table 3 and the 5.5 GHz light curve of AT2022dsb is plotted in Fig. 7 along with a selection of other radio-detected TDEs for comparison. Both the variability of the detected 5.5 and 9 GHz radio emission and that the initial detection is above the 3σ VLASS 3 GHz upper limits years prior to the TDE suggest that the radio emission is likely related to the transient event and is not purely host galaxy emission. Although this VLASS upper limit is at a lower frequency than the ATCA observations (5.5 and 9.0 GHz), the ATCA spectrum is steep in the first epoch, so a spectral turnover would be needed in order to match the VLASS upper limit, which is not consistent with the host galaxy emission (that should be steep).

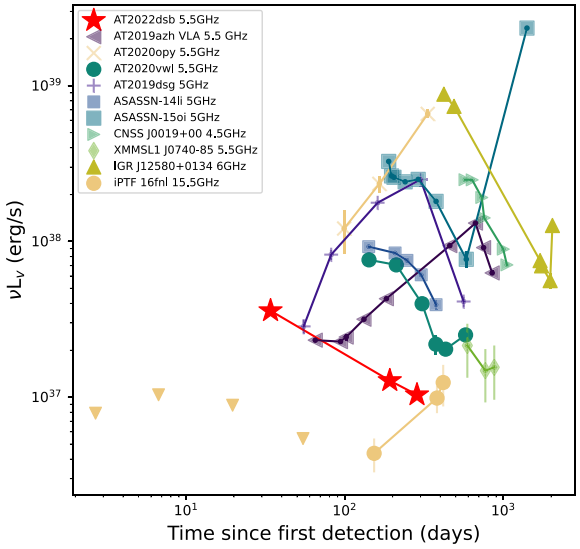

Figure 7. 5.5 GHz radio luminosity of AT2022dsb (red stars) compared to a selection of other radio-detected thermal TDEs (AT 2019azh; Goodwin et al. 2022a; AT 2020opy; Goodwin et al. 2022b; AT 2019dsg; Cendes et al. 2021; ASASSN 14li; Alexander et al. 2016; ASASSN 15oi; Horesh, Cenko & Arcavi 2021; CNSS J0019+00; Anderson et al. 2020; XMMSL1 J0740−85; Alexander et al. 2017; IGR J12580+0134; Irwin et al. 2018; AT2020vwl; Goodwin et al. 2023; AT2018hyz; Cendes et al. 2022). The horizontal axis indicates the time since first detection of the source at optical or X-ray wavelengths.

4 DATA ANALYSIS

4.1 X-ray spectral fitting

The X-ray spectra were analysed using the Bayesian X-ray Analysis software (BXA; Buchner et al. 2014), which connects the nested sampling algorithm ULTRANEST[10] (Buchner 2021) with the fitting environment CIAO/Sherpa (Fruscione et al. 2006). The eROSITA and *XMM* PN spectra were fitted in the 0.2–8 keV and 0.2–10 keV range, respectively. A joint fit of the source and background spectra was performed, using the C-statistic for fitting (Cash 1976), and modelling the background using the principal component analysis (PCA) technique described in Simmonds et al. (2018). The Galactic absorption is modelled with a total (H I and H_2) Galactic hydrogen column density of 1.73×10^{21} cm^{-2} (Willingale et al. 2013), cosmic abundances from Wilms, Allen & McCray (2000) and cross-sections from Verner et al. (1996).

Each of the eROSITA and *XMM* PN spectra were fitted with the following source models, commonly used to fit the X-ray spectra of TDEs: (i) `zbbody`: redshifted blackbody (ii) `zpowerlaw`: redshifted power law, (iii) `zbremsstrahlung`: redshifted thermal bremsstrahlung. To assess the goodness of fit and compare between different fitted models, we use the Akaike Information Criterion (*AIC*), defined as $AIC = 2k - 2\ln\hat{\mathcal{L}}$, where k is the number of free-parameters in the fitted model, and $\hat{\mathcal{L}}$ the estimated maximum likelihood from the spectrum fitting; the lower the value of the AIC, the better the fit to the spectrum. An overview of the spectral fit parameters are listed in Table 4.

The eRASS5 spectrum, obtained ∼14 d before the optical peak, is ultra-soft, and can be well fitted by the thermal bremsstrahlung model with temperature $kT_{\rm brems} = 71^{+8}_{-5}$ eV (Fig. 8), or a blackbody

[10] https://johannesbuchner.github.io/UltraNest/

Table 4. X-ray spectral fit results. The Akaike Information Criterion (*AIC*) column estimates the goodness of fit, with a lower *AIC* representing a better fit.

MJD	ObsID	zbbody		zpowerlaw		zbremsstrahlung	
		AIC	kT [eV]	AIC	Γ	AIC	$kT_{\rm brems}$ [eV]
59 627.939	eRASS5	367.6	47^{+5}_{-5}	367.9	$7.7^{+0.2}_{-0.4}$	366.8	71^{+8}_{-5}
59 646.226	XMM1	9908.3	219^{+28}_{-24}	9893.8	$2.7^{+0.3}_{-0.3}$	9899.7	768^{+346}_{-173}
59 820.520	XMM2	7925.8	150^{+26}_{-23}	7918.0	$3.5^{+0.5}_{-0.5}$	7921.1	403^{+155}_{-96}

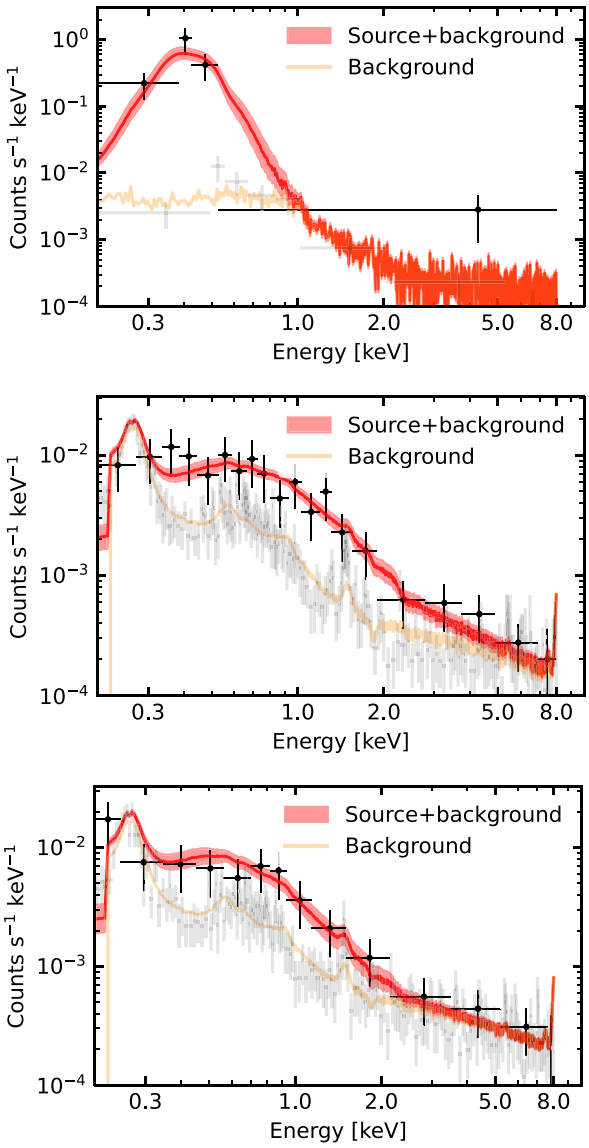

Figure 8. BXA fitted models to the convolved X-ray spectra from eROSITA (top, 14 d before optical peak) and *XMM* (bottom two plots, ∼5 and ∼180 d after optical peak). Black and grey markers represent source and scaled background spectra, respectively, with the background component not originating from the TDE host galaxy. The solid red line denotes the median model, whilst the shaded red band encloses 68 per cent of the posterior. The preferred model (Table 4) for the eRASS5 spectrum is thermal bremsstrahlung with $kT_{\rm brems} = 71^{+8}_{-5}$ eV, whilst it is a power law for the *XMM* spectra, with Γ of $2.7^{+0.3}_{-0.3}$ and $3.5^{+0.5}_{-0.5}$, respectively. The unconvolved models and spectra are presented in Fig. 9.

with temperature $kT_{\rm bb} = 47^{+5}_{-5}$ eV; such temperatures are consistent with the X-ray spectra of other X-ray bright thermal TDEs (e.g. Saxton et al. 2020). This corresponds to a 0.2–2 keV observed flux, $F_{\rm X,\,obs} = (3.4^{+0.6}_{-0.5}) \times 10^{-13}$ erg cm^{-2} s^{-1}, and a 0.2–2 keV unabsorbed flux, $F_{\rm X,\,unabs} = (1.6^{+0.4}_{-0.4}) \times 10^{-11}$ erg cm^{-2} s^{-1}($L_{\rm X} = 2.5^{+0.6}_{-0.5} \times 10^{43}$ erg s^{-1}).

The first *XMM* PN spectrum, taken ∼19 d after the eRASS5 spectrum, is harder, and can be best-fit by a power law with photon index $2.7^{+0.3}_{-0.3}$. The eRASS5 to XMM spectral hardening is also accompanied by a factor of ∼39 decrease in $F_{\rm X,\,obs}$ to $(8.9^{+2.3}_{-1.8}) \times 10^{-15}$ erg cm^{-2} s^{-1}. The early-time evolution of the spectral energy distribution (SED) evolution between the eROSITA and *XMM* observation is plotted in Fig. 9. At ∼173 (∼154) d after the eRASS5 (first *XMM* observation), the second *XMM* observation shows a power-law slope consistent with the first *XMM* observation with photon index $3.5^{+0.5}_{-0.5}$, as well as a similar observed 0.2–2 keV flux of $(6.6^{+1.3}_{-1.1}) \times 10^{-15}$ erg cm^{-2} s^{-1}. The 0.2–2 keV fluxes in these *XMM* observations are below the 3σ upper limit inferred from the stacked eROSITA observations from its first four all-sky surveys (Section 2), such that it would not have been possible to have detected this harder power-law component if it were present in the eRASS5 observation.

The photon index of $\Gamma \sim 2.7$ in the first *XMM* observation is much softer than the photon indices of X-ray bright AGN; for example, Nandra & Pounds (1994) characterized a sample of continuum slopes of Seyfert galaxies by a Gaussian with 1.95 ± 0.15. In addition, it is also softer than the hard X-ray emission from an advection-dominated accretion flow (ADAF; e.g. Narayan, Mahadevan & Quataert 1998) of slope $\lesssim$2 (Gu & Cao 2009), yet harder than the spectra of thermal TDEs (Saxton et al. 2021). With a 0.2–2 keV luminosity of $\sim 4 \times 10^{40}$ erg s^{-1} and with no major change in flux in the 0.2–2 keV band between the two *XMM* epochs, we consider the *XMM* source spectra to be likely dominated by diffuse X-ray emission from within the circumnuclear environment of the host galaxy (i.e. unrelated to the TDE-triggered accretion episode onto the SMBH). This is in part motivated by the host galaxy of AT 2022dsb likely hosting a LLAGN prior to its 2022 outburst (recall the mid-infrared colour of $W1$–$W2 \sim 0$ and previous type II AGN classification for its host galaxy; Section 2), with past X-ray observations of nearby LLAGN also suggesting the presence of hot, diffuse plasma within a few hundred parsecs of the nucleus (Flohic et al. 2006), and with $\log[L_{0.5-2\,\rm keV}]$ and $\log[L_{2-10\,\rm keV}]$ luminosities in the range of 40.2 ± 1.3 and 39.9 ± 1.3 (González-Martín et al. 2009).

A similar scenario may also have been present in the TDE candidate ASASSN-15oi (Gezari, Cenko & Arcavi 2017), where two *XMM* spectra, taken ∼80 and ∼230 d after optical discovery, were best fitted[11] by a two component model consisting of a blackbody with $kT = 47 \pm 3$ eV and a power law with $\Gamma = 2.5 \pm 0.8$. As ASASSN-15oi brightened in the X-rays over the ∼160 d between

[11] These spectral fit results are reported in Gezari et al. 2017 and were obtained using the first *XMM* spectrum.

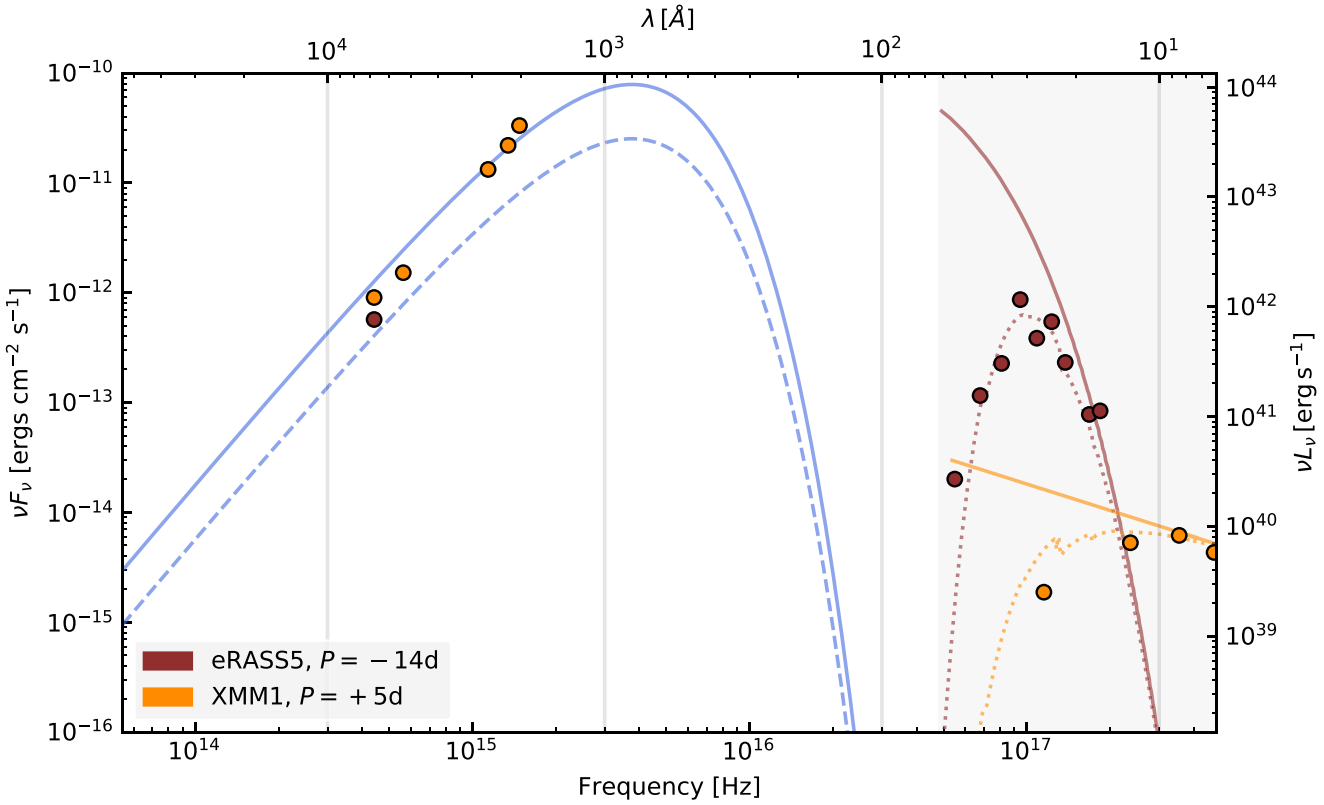

Figure 9. Early SED evolution of AT 2022dsb. The red and orange markers show the SED near the time of the eRASS5 detection (MJD ∼ 59 627, 14 d before optical peak) and first *XMM* observation ∼19 d later (MJD ∼ 59 646, 5 d after optical peak). The dotted and solid lines in the X-ray band-pass (grey region) denote the observed and unabsorbed best-fitting spectral models. The solid blue line passing through the optical-UV data points (orange markers) represents the best-fitting blackbody function to photometric observations performed around the time of the *XMM* observation (Section 4.2), with $T_{\rm BB} = (4.6 \pm 0.7) \times 10^4$ K, and of a lower temperature than the blackbody fitted to the X-ray spectrum in eRASS5 ($kT = 47 \pm 5$ eV, or $\sim 5 \times 10^5$ K; Table 4). The blue dashed line represents a blackbody function with $T_{\rm BB} = 4.6 \times 10^4$ K, but with its luminosity rescaled based on the ratio of fluxes at phases −14 and +5 d when modelling the optical flux evolution with the half-Gaussian presented in Fig. 11 (a rescaling is performed here due to only ATLAS photometry being available around the time of the eRASS5 observation).

these spectra, only the normalization of the blackbody component increased, without a significant change in kT or Γ. This would require a fair amount of model fine-tuning if the power-law component originated from Compton upscattered TDE disc photons, and the disc luminosity varied over time. Instead, this may be more easily explained if the disc emission evolves independently of the lower luminosity diffuse host emission (as also suggested in Gezari et al. 2017), with the latter being emitted at much larger physical length scales than the X-ray emission from the TDE disc.

If the *XMM* source spectra are dominated by the diffuse emission with the host galaxy, then the soft X-ray emission dominating the eRASS5 spectrum may have been obscured by optically thick material (see Section 6 for further discussion on its possible origin). Assuming that the TDE disc has spectral properties in its first *XMM* spectrum similar to eRASS5 ($kT_{\rm BB} \sim 50$ eV) and a similar blackbody normalization, then an increase in the neutral hydrogen column density along our line-of-sight to $>4.9 \times 10^{21}$ cm^{-2} would be capable of causing a 0.2'2 keV flux drop by a factor of at least 39 (between these two spectra), or a He II column density of 1.6×10^{21} cm^{-2} if the flux drop is due to photoionization of He II (Fig. 10), when modelling He II absorption[12] using the `xspec` model `ISMabs` (Gatuzz et al. 2015). The conversion of these column densities into an estimate of the mass of a debris envelope obscuring the disc is complicated by the unknown ionization fraction of helium in the debris; an alternate approach to constrain the reprocessor's properties at early times is presented in Section 6.

[12]The column densities of all other species are set to zero within this absorption model here.

4.2 Photometric analysis

Following Malyali et al. (2023b), the ATLAS *o*-band light curves were fitted with a half-Gaussian rise, exponential decay model, as described in Velzen et al. (2019), and plotted in Fig. 11. Only the *o*-band photometry was fitted here due to this providing the best sampling of the rise and decay of the optical emission, and only photometry in the range 59 600 < MJD < 59 750 was used. The inferred rise and decay time-scales are $\sigma = 7.9^{+0.4}_{-0.4}$ d and $\tau = 21.0^{+0.6}_{-0.6}$ d, respectively, with the light curve peaking at MJD $= 59640.9^{+0.5}_{-0.4}$; this value is used as the reference time for the optical peak of AT 2022dsb in this work. The peak inferred F_ν is 320^{+7}_{-6} μJy, corresponding to $\nu L_\nu \sim 2 \times 10^{42}$ erg s^{-1}. To help understand when the eRASS5 detection occurs during the evolution of the TDE, then it is also valuable to define a start time for the optical rise based on the fitted model here. If one considers this to be when the optical flux is ∼1 per cent (∼0.03 %) of the optical peak, then this would occur when MJD$_{\rm start}$ ∼59 617 (∼59 609).

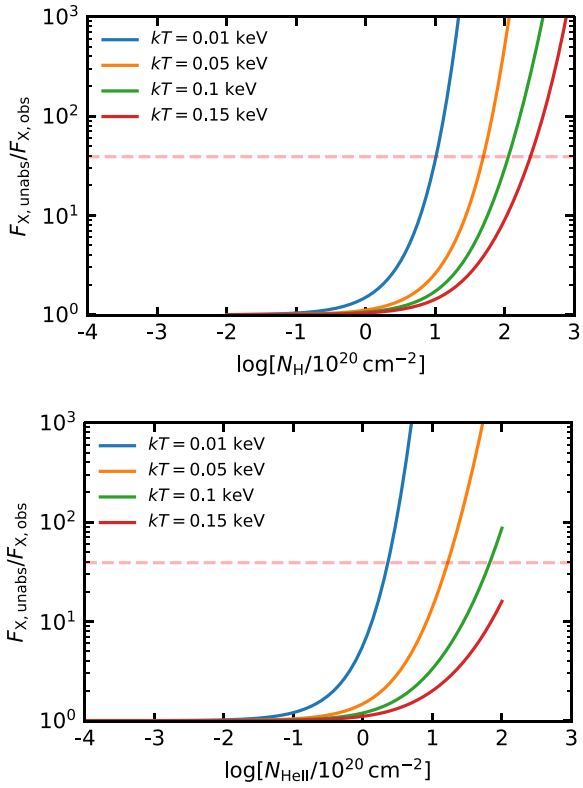

Figure 10. The amplitude of the observed flux drop in the 0.2–2 keV band ($F_{X,\,unabs}/F_{X,\,obs}$) due to absorption by neutral hydrogen (top) and He II (bottom), with each curve representing a different blackbody temperature ($kT \sim 0.05$ keV for AT 2022dsb). The sensitivity of $F_{X,\,unabs}/F_{X,\,obs}$ to absorption depending on the balance between the ionization potential of the absorber and kT. The horizontal red dashed line corresponds to the flux drop by a factor of 39 at early times seen in AT 2022dsb, corresponding to an N_H ($N_{He\,II}$) of 4.9×10^{21} cm^{-2} (1.6×10^{21} cm^{-2}).

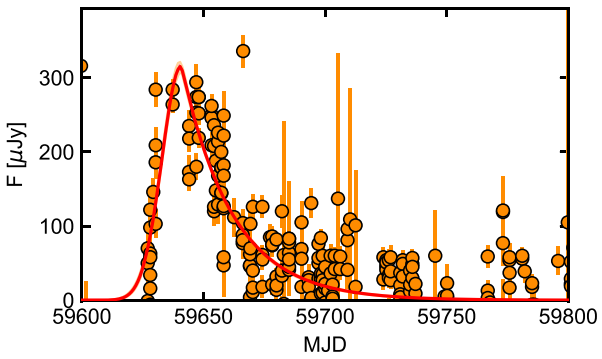

Figure 11. Half-Gaussian rise, exponential decay model (red) fitted to the ATLAS *o*-band photometry (orange markers). The shaded red bands denote the credible region enclosed by the 16th and 84th percentiles of the posterior. The data point with $F \sim 300\,\mu$Jy at MJD $\sim$ 59 600 has a 1σ error consistent with 0 (i.e. is not precursor emission to the main flare).

To obtain a more physically motivated estimate of the start time of the event, then we also fitted the multiband photometry (ATLAS *o* and *c*, ZTF *g* and *r*, *Swift UVW1*, *UVM2* and *UVW2* bands; Fig. 12) with the TDE module (Mockler et al. 2019) of the Modular OpenSource Fitter for Transients (MOSFIT; Guillochon et al. 2018), using the nested sampler DYNESTY for posterior sampling (Speagle 2020). The free parameters of this model are the black hole mass (M_{BH}), mass of the disrupted star ($M_\star$), the scaled impact parameter (b), the efficiency of converting accretion luminosity into the optical luminosity (ϵ), a normalizing factor and exponent for the photosphere radius ($R_{ph,\,0}$, l_{ph}), a viscous delay timescale ($T_{viscous}$) and the time of first mass fall back to pericentre (MJD_{fb}). Although most of the inferred parameter estimates are dominated by systematics (Table 5), we note that the MOSFIT modelling does suggest a lower mass SMBH for the disruption with $\log[M_{BH}/M_\odot] = (6.4^{+0.2}_{-0.2})\pm0.2$, as compared to the black hole mass, $\log[M_{BH}/M_\odot] = 7.3^{+0.2}_{-0.3}$, derived from the M_{BH}– $M_{\star,\,gal}$ relation (Reines & Volonteri 2015) using $M_{\star,\,gal}$ from the host galaxy SED analysis (Section 2). The inferred $MJD_{fb} = (59610.2^{+6.6}_{-6.3}) \pm 15$ is consistent with the start time for the optical rise inferred above.

In addition, we used the SUPERBOL package (Nicholl 2018) to infer the luminosity (L_{BB}) evolution of a blackbody function fitted to the multi-epoch optical-UV photometry. This involved first interpolating the ATLAS and *Swift* UVW1, UVM2 photometry onto MJDs where *Swift* UVW2 observations were performed, before fitting a blackbody to the multiband photometry and computing L_{BB} via integration of the best-fitting model. The evolution of L_{BB}, the blackbody temperature, T_{BB}, and the blackbody radius, R_{BB} is plotted in Fig. 13, whilst the SED at early times is shown in Fig. 9. T_{BB} and R_{BB} range between 1.9–4.6 $\times$ 10^4 K, and 1.2–3.0 $\times$ 10^{14} cm, with median values of 2.4 $\times$ 10^4 K and 1.8 $\times$ 10^{14} cm, respectively; the evolution of T_{BB} and R_{BB} is broadly consistent with the population of optically selected TDEs (e.g. Hammerstein et al. 2023). In Fig. 14, we plot the evolution of the L_{BB}/L_X ratio, where L_X is the rest-frame 0.2–2 keV luminosity corrected for Galactic absorption. At $\sim$14 d before optical peak, then $\log[L_{BB}/L_X] = 0.3 \pm 0.3$, but increases to 3.5 ± 0.2 $\sim$19 d later, with such an extreme increase in L_{BB}/L_X yet to have been observed at early times in a TDE before (Hammerstein et al. 2023; see Section 5).

4.3 Spectroscopic analysis

We used a modified version of the PYTHON quasar fitting code (PYQSOFIT; Guo, Shen & Wang 2018) to fit the optical spectra of AT 2022dsb after dereddening the Galactic foreground contribution. First, we fitted the emission line free regions of each of the optical spectra with a power law to estimate the continuum contribution to the spectrum, before dividing the observed spectrum by this continuum component to obtain a normalized spectrum. We note that we do not attempt to model or subtract the host galaxy component here, such that the modelled continuum involves both TDE and host galaxy emission. All spectral fitting made use of the PYTHON package LMFIT (Newville et al. 2014) and the Markov Chain Monte Carlo (MCMC) sampler EMCEE (Foreman-Mackey et al. 2013).

After normalizing by the continuum, we fitted each of the narrow emission lines in this complex (H α, [N II] 6548 and 6583 Å) with a single Gaussian, and forced each of these to be of the same width. The broad H α component was fit with a single Gaussian (Fig. 15). Due to the possible presence and blending of emission from H β, He II 4686, N III 4640 Å, H γ, Fe II 37, 38, within the broad He II complex, it is not straightforward to constrain the evolution of each of these possible components; we therefore examine the more isolated broad H α emission lines here.

In the first LCO FLOYDS spectrum obtained $\sim$5 d before optical peak, the full-width half max (FWHM) of the broad H α line is 10400 $\pm$ 400 km s^{-1}, and its centroid is blueshifted to λ_{rest} =6530 $\pm$ 7 Å, corresponding to a velocity of -1600 ± 300 km s^{-1}. In the second optical spectrum obtained $\sim$1 d

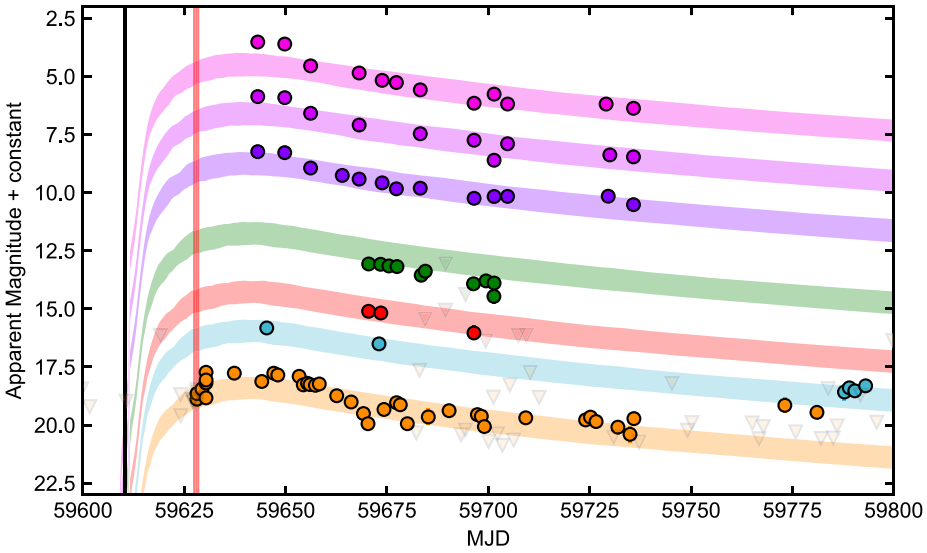

Figure 12. MOSFIT model fits to the multiband photometry of AT 2022dsb, with colour scheme following Fig. 3. The black and red lines mark the estimated median time of first mass fallback ($MJD_{fb} = 59\,610 \pm 6$) and the eRASS5 coverage of AT 2022dsb, occurring only ∼17 d later. A zoom-in on the ATLAS *o*-band difference photometry sampling the optical rise, and which is used for constraining MJD_{fb}, is presented in Fig. 11.

Table 5. Posterior medians and 1σ credible regions inferred from the MOSFiT TDE light curve fitting. The estimated systematic errors on each estimate are taken from Mockler, Guillochon & Ramirez-Ruiz (2019).

Parameter	Value	Systematic Error
$\log(M_{bh}/M_\odot)$	$6.4^{+0.2}_{-0.2}$	±0.2
$\log(M_\star/M_\odot)$	$0.2^{+0.3}_{-0.1}$	±0.66
b	$1.0^{+0.2}_{-0.3}$	±0.35
$\log(\epsilon)$	$-2.0^{+0.5}_{-0.5}$	±0.68
$\log(R_{ph,0})$	$-0.1^{+0.3}_{-0.3}$	±0.4
l_{ph}	$1.0^{+0.2}_{-0.2}$	±0.2
$\log(T_{viscous}/days)$	$-0.9^{+1.1}_{-1.2}$	±0.1
MJD_{fb}	$59610.2^{+6.6}_{-6.3}$	±15

before optical peak, the FWHM is $10\,500 \pm 300\,km\,s^{-1}$, consistent with the earlier spectrum, but the velocity offset is $200 \pm 400\,km\,s^{-1}$. At later times, the Hα emission line is not clearly seen above the host galaxy continuum emission.

5 EARLY-TIME X-RAY EMISSION IN TDES

In the following section, we briefly review the literature on early-time X-ray observations of TDEs, and compare the X-ray transient seen in AT 2022dsb (Fig. 3) with the wider TDE population.

The majority of the X-ray selected TDE population known prior to the launch of eROSITA was first discovered at a time when wide-field high-cadence optical surveys were still relatively limited compared with the current generation, with respect to their depth, cadence, sky coverage, difference-imaging capabilities (important for nuclear transients), and ease-of-access to their optical light curves. Largely as a result of this, only a handful of the X-ray selected TDE candidates showed transient optical/ UV emission (Saxton et al. 2020), which was only ever identified after the initial X-ray discovery, and typically only through *Swift* UVOT follow-up. Furthermore, of the systems with detected transient optical/ UV emission, only the decaying phase of the TDE light curve was sampled in the UV (see discussion in section 9 in a recent review Saxton et al. 2020), thus the early-time X-ray evolution (during the initial optical/ UV brightening) of these X-ray selected systems remains unknown. Whilst the launch of eROSITA has seen a vast increase in the number of X-ray bright TDE candidates (e.g. Malyali et al. 2021; Homan et al. 2023; Liu et al. 2023; Malyali et al. 2023a, b), the majority of the TDE candidate population show no transient optical emission. In a sample of eROSITA-selected TDE candidates (Sazonov et al. 2021), only four systems display both transient X-ray and optical emission, but the detections of flaring X-ray emission associated to the TDE always occurs after the optical peak.

Although the number of optically selected TDE candidates has rapidly increased over the last decade, the majority of these have X-ray observations commencing at earliest near to, or after, peak optical brightness. This may in part stem from the very high discovery rate of transients in the latest generation of optical surveys, meaning that astronomers generally wait until close to peak optical brightness for an optical transient to become a strong TDE candidate, and only then trigger X-ray follow-up observations. Despite this, there are still six optically bright TDEs with X-ray observations starting before optical maximum (Table 6 and Fig. 16), where this list was obtained via visual inspection of the joint X-ray and optical light curves of the TDEs presented in both the ZTF TDE sample (Hammerstein et al. 2023), and those in the recent TDE review paper by Gezari (2021). All of these TDEs are of H + He type,[13] with the exception of AT 2019ahk, which only shows transient broad Balmer emission lines. For each of these systems, the 0.3–2 keV XRT light curves were generated and downloaded from the UKSSDC as in Section 3.1.3. These were then converted to 0.2–2 keV light curves using webPIMMS, assuming a redshifted blackbody spectrum with $kT = 50$ eV (similar to other X-ray bright TDEs; Saxton et al. 2020), absorbed by a Galactic N_H along the line-of-sight to the TDE taken

[13]This is likely due current TDE follow-up strategies, since if a He complex is detected in a follow-up optical spectrum obtained during the optical rise, then there's a stronger indication that the event is a TDE at these early times, and a higher likelihood of *Swift* XRT and UVOT observations being triggered with high urgency to monitor the evolution of the system.

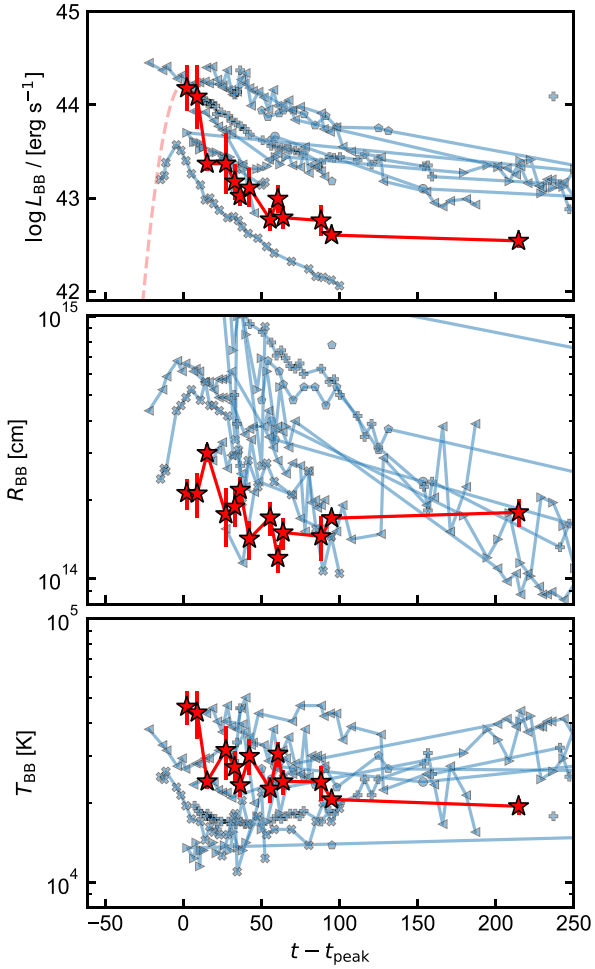

Figure 13. Evolution of the blackbody emission inferred from fitting the optical and UV photometry of AT 2022dsb (red stars). The red dashed line in the top panel represents the approximated rise in L_{BB} when scaling the optical emission with the half-Gaussian rise presented in Fig. 11, assuming a constant temperature. The blue background data points represent the blackbody evolution for a subset of optically selected TDEs in Hinkle et al. (2021), which also have a time of peak optical brightness quoted in Hammerstein et al. (2023).

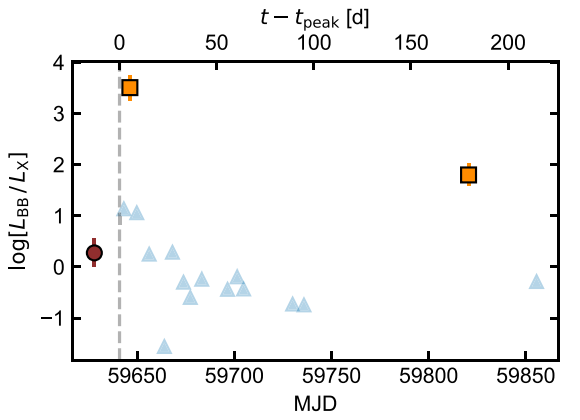

Figure 14. Time evolution in the ratio of the bolometric blackbody luminosity, L_{BB}, to the rest-frame 0.2–2 keV luminosity corrected for Galactic absorption, L_X. At ∼14 d before optical peak, then $\log[L_{BB}/L_X] = 0.3 \pm 0.3$, but increases to 3.5 ± 0.2 ∼19 d later. The markers are the same as in Fig. 3, with the exception that the triangles represent 3σ lower limits.

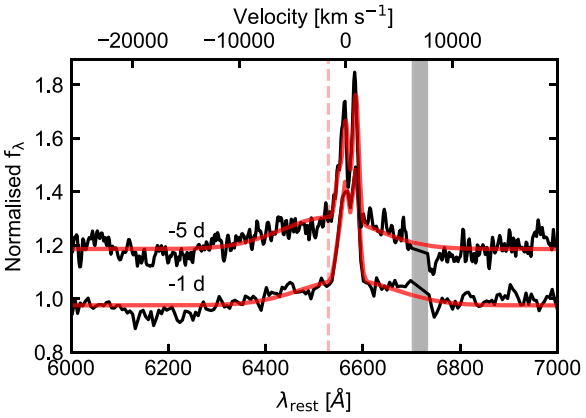

Figure 15. Fits to the H α complex for the first two optical spectra obtained at 5 and 1 d before optical peak. The continuum normalized spectra are shown in black and offset for clarity, with the best-fitting models in red. The grey band denotes a region of telluric absorption which was masked during fitting. The centroid of the broad H α in the spectrum taken 5 d before optical peak is marked with a red dashed vertical line, and is shifted by -1600 ± 300 km s^{-1} with respect to the rest frame of the host galaxy (Section 4.3).

from Willingale et al. (2013); lower kT values for each TDE here would lead to higher estimated 0.2–2 keV fluxes.

Comparing the X-ray light curve of AT 2022dsb with the other TDEs with pre-peak X-ray observations (Fig. 16), then it is clear that the early-time transient X-ray emission in AT 2022dsb has never been observed before across all known TDEs with well sampled optical peaks. Of the TDEs in Table 6, only AT 2019azh has a significant detection of soft X-ray emission before the observed optical maximum, with the system being detected for the first time ∼3 d before optical peak. AT 2019azh then remains at approximately a constant L_X over the following ∼40 d after the first significant detection (Fig. 16), and thus shows a vastly different X-ray evolution to AT 2022dsb.

We note that we have not included the TDE candidate AT 2019dsg (Cannizzaro et al. 2021; Stein et al. 2021) in this comparison primarily because the first X-ray observations of this system commenced ∼19 d after optical peak, although its properties are worth briefly discussing. AT2019dsg was initially detected as an ultra-soft X-ray source (blackbody spectrum with $kT = 72 \pm 5$ eV, 0.2–2 keV peak observed $L_X = (2.8 \pm 0.3) \times 10^{43}$ erg s^{-1}), which later dimmed by a factor of ∼50 in its soft X-ray flux over the following 160 d after the first X-ray observation of the system. The X-ray decline in AT 2019dsg thus evolves on slower time-scales, and importantly, at a much later time with respect to optical peak than in AT 2022dsb. A number of other TDEs have shown large amplitude X-ray flux declines in their light curves post-optical peak (e.g. fig. 14 in Malyali et al. 2023b). AT 2019dsg was also classified as a H + He TDE (Velzen et al. 2021) and showed transient radio emission (Cendes et al. 2021), but the 5 GHz radio evolution of AT 2019dsg also continued to brighten up until ∼200 d after disruption, contrasting the early radio transient emission seen in AT 2022dsb (Fig. 7).

The eRASS5 observation is not the earliest X-ray observation of a TDE in terms of the phase (number of days observed before optical maximum), with AT 2018dyb, AT 2019ahk, AT 2019azh, and AT 2020zso all having been observed at earlier phases than AT 2022dsb. Furthermore, each of the earliest time observations for each system should also have been able to detect AT 2022dsb-like X-ray emission, given the 3σ upper limits on L_X were lower than the L_X of the eRASS5 observation of AT 2022dsb. However, the optical-UV light curves of

Table 6. Properties of TDEs with X-ray observations pre-optical peak. MJD_{peak} is the inferred optical peak, L_X^{1st} is the inferred 3σ upper limit on the 0.2–2 keV luminosity from the earliest X-ray observation (by *Swift* XRT) and P denotes the phase of the first X-ray observation relative to MJD_{peak}. σ is the inferred rise timescale from a half-Gaussian fitted to the optical light curve (Section 4.2). MJD_{peak} and σ were taken from Velzen et al. (2020) for iPTF15af, AT 2018dyb, AT 2019ahk, AT 2019azh, AT 2019qiz, and Hammerstein et al. (2023) for AT 2020zso.

Name	MJD_{peak}	L_X^{1st} [erg s^{-1}]	P [d]	σ [d]	P/σ
AT2018dyb	$58340.7^{+1.4}_{-1.3}$	$<7 \times 10^{42}$	−23.1	$31.6^{+2.3}_{-0.7}$	−0.7
AT2019ahk	$58548.3^{+0.8}_{-0.9}$	$<3 \times 10^{42}$	−33.5	$20.0^{+0.5}_{-0.5}$	−1.7
iPTF15af	$57061.0^{+1.6}_{-1.8}$	$<2 \times 10^{43}$	−11.7	$31.6^{+1.5}_{-2.1}$	−0.4
AT2019azh	$58558.6^{+1.5}_{-1.6}$	$<1 \times 10^{42}$	−13.8	$20.0^{+2.4}_{-1.3}$	−0.7
AT2019qiz	$58761.4^{+0.6}_{-0.6}$	$<1 \times 10^{42}$	−8.3	$6.3^{+0.1}_{-0.1}$	−1.3
AT2020zso	$59188.0^{+1.4}_{-1.4}$	$<4 \times 10^{43}$	−15.0	$6.9^{+0.2}_{-0.2}$	−2.2
AT2022dsb	$59640.9^{+0.5}_{-0.4}$	$2.5^{+0.6}_{-0.5} \times 10^{43}$	−13.5	$7.9^{+0.4}_{-0.4}$	−1.7

these TDEs evolve differently to AT 2022dsb, with respect to their peak luminosities and rise time-scales. This is not unexpected, since these systems may span a range of different black hole masses, stellar masses, and impact parameters. For example, the rise time-scale of AT 2022dsb is inferred to be ∼8 d, whereas it is ∼31 d for iPTF-15af (Velzen et al. 2020) (Table 6). This complicates a clean comparison between these systems, and the task of understanding how early on in a TDE's evolution an AT 2022dsb-like X-ray transient may be observable. If one considers the normalized phase (phase divided by the estimated rise time-scale; Table 6), then the eRASS5 observation of AT 2022dsb represents the second earliest X-ray observation of a TDE showing a transient He II emission complex, with only AT 2020zso being observed at an earlier stage of the lightcurve.

Whilst the detection of the early-time X-ray transient in AT 2022dsb certainly benefitted from eROSITA serendipitously scanning over it a day before the first optical detection, this cannot be the sole factor in this discovery given the XRT coverage of other TDEs described above (i.e. there were observations that were early and deep enough to detect a source with spectral properties similar to AT 2022dsb, but did not because of physical differences between these systems). The fact that the X-ray emission could have been observed in other TDEs but was not, particularly for AT 2020zso (the TDE with observations performed at the earliest normed phase), suggests that the assumptions made when converting the observed 0.3–2 keV XRT count rate into an unabsorbed 0.2–2 keV flux (corrected only for Galactic absorption), and then a 0.2–2 keV intrinsic luminosity, may have been oversimplified and require further consideration. For example, an additional absorber along the line-of-sight to the TDE disc (such as from stellar debris ejected during the circularization process, which may be optically thick or thin depending on the observer's viewing angle to the system, or from neutral hydrogen in the host galaxy unrelated to the TDE), or a lower effective temperature of the disc emission (e.g. due to a retrograde black hole spin), would lead to larger estimated unabsorbed flux upper limits from the XRT observations, and might explain the previous non-detections of X-ray emission in these systems. The early-time X-ray transient seen in AT 2022dsb is likely not a universally observable feature in TDEs.

6 DISCUSSION

The unique observational feature of AT 2022dsb with respect to the wider population of optically selected TDEs is its early-time transient X-ray emission detected by eROSITA (see Table 7 for a summary of the key events in the evolution of AT 2022dsb). From the physical modelling of the multiband photometry (Section 4.2), then the time of first mass fallback to pericentre after the disruption is estimated to be MJD ∼ 59 610 (∼31 d before optical peak), meaning that the eROSITA discovery of ultra-soft X-ray emission on MJD 59 627 occurs only 17 d after this. As the optical emission brightens in the system, then the observed X-ray emission in the 0.2–2 keV band decays over a 19 d period by a factor of ∼39 (Fig. 3). This joint X-ray-to-optical evolution has not been observed before in a TDE candidate. Although the observed X-ray emission rapidly dims during the optical rise, AT 2022dsb shows a broad He II complex which persists for at least ∼38 d after optical peak, and was first detected 5 d before peak (Fig. 6). Several outflow signatures are also present during the early stages of this TDE, in the form of blueshifted H α at -1600 ± 300 km s^{-1}, first observed at $P = -5$ d (Section 4.1), radio transient emission at $P = 20$ d (Fig. 7), and blueshifted Ly α absorption lines at ∼3000 km s^{-1}, observed at $P =$ 54 d (Engelthaler & Maksym 2023, Engelthaler et al. in preparation). Importantly, other past X-ray observations of He-TDEs before optical peak have not detected X-ray emission at a similar L_X (Table 6), despite the observations being carried out at a similar phase to the eRASS5 observation of AT 2022dsb, and also having upper limits on L_X lower than for the eRASS5 detection of AT 2022dsb; each of the He TDEs in this sample have also been reported to show outflow signatures in observations performed around optical peak (Table 8).

The early X-ray emission detected by eROSITA likely comes from an accretion disc that has recently been assembled through circularization of the earliest-arriving gas in the fallback stream (Bonnerot, Lu & Hopkins 2021). We rule out the early X-ray transient being produced by shock breakout emission from the surface of the star after being maximally compressed at pericentre (Carter & Luminet 1983; Guillochon et al. 2009; Stone, Sari & Loeb 2013; Yalinewich et al. 2019), as the predicted time-scales of $\mathcal{O}$(minutes) for these flares are far shorter than what is observed in the eRASS5 observation (>1 d; Fig. 5). We also disfavour the X-ray transient being caused by accretion disc cooling (e.g. Cannizzaro et al. 2021), since the disc temperature should increase as the optical emission brightens if the optical light curve traces the accretion rate at early times, or Lense–Thirring driven precession of the newly formed disc (Stone & Loeb 2012; Franchini, Lodato & Facchini 2016), as no rebrightening episodes are detected over the X-ray follow-up campaign (Fig. 3). Regardless of origin, then the high-energy tail of this early hard ionizing source also likely drives the ionization of He II and the formation of the He-complex in the optical spectra.

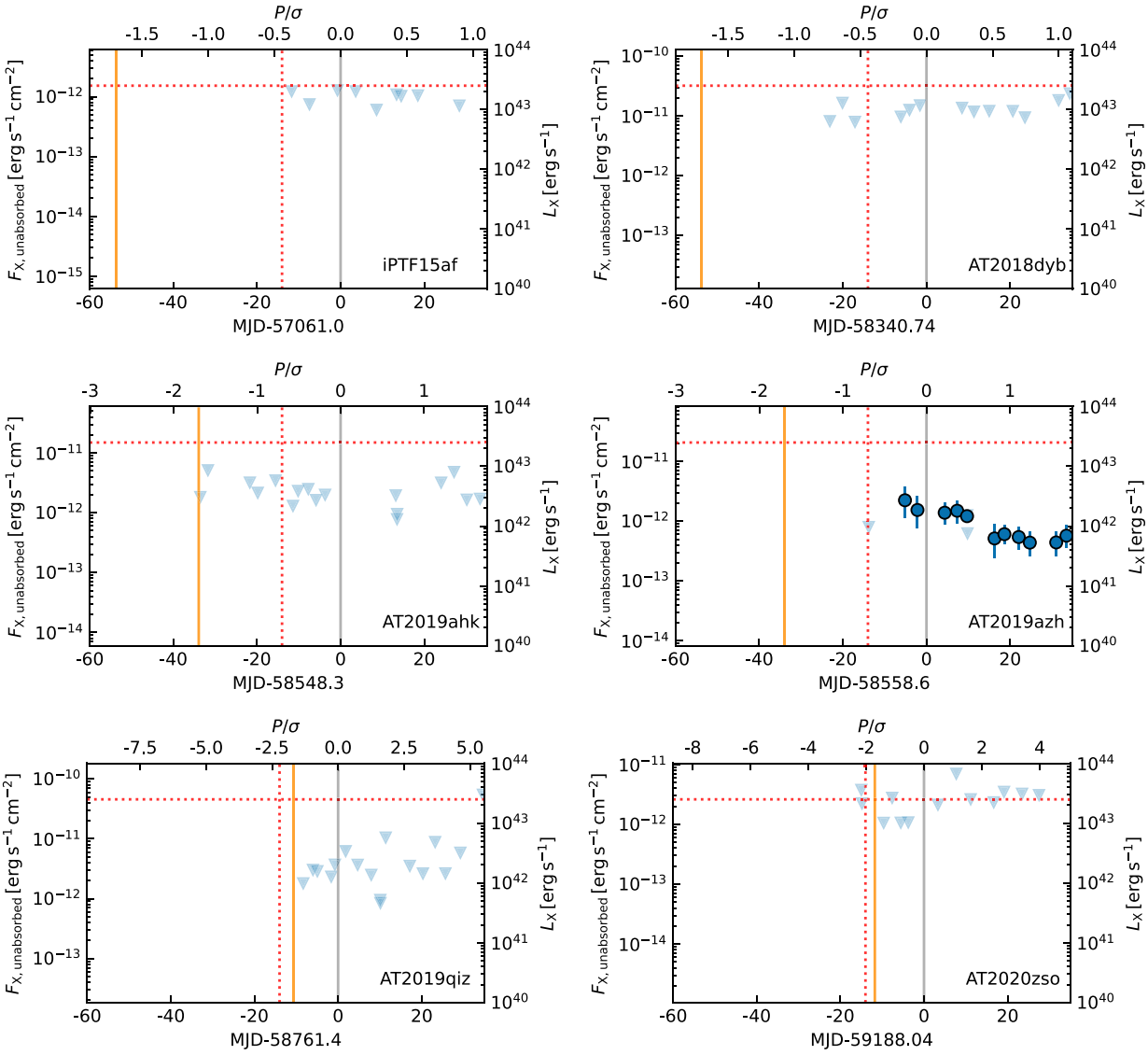

Figure 16. Early-time X-ray light curves of TDEs with observations pre-optical peak, with markers following the same definition as for Fig. 3. The dotted red lines mark the phase of the eRASS5 observation of AT 2022dsb and inferred 0.2–2 keV luminosity, whilst the dark orange solid line marks the eRASS5 observation at the time of its normed phase, P/σ (Table 6). MJDs are defined with respect to the inferred optical peaks in Table 6. The eROSITA observation clearly represents the earliest X-ray detection of a TDE to date, and although there are XRT observations of these other TDEs at a comparable phase, only AT 2020zso has been observed at an earlier P/σ.

Table 7. Key events in the early evolution of AT 2022dsb.

MJD	Event
∼59610	Time of first mass fallback to pericentre (Section 4.2).
59 627	eRASS5 detection.
59 628	First 3σ detection of optical emission in ATLAS *o*-band.
59 636	Broad blueshifted H α and an emission complex detected around He II 4686Å , in the first follow-up optical spectrum of AT 2022dsb.
59 641	Peak in the observed optical flux (Section 4.2).
59 646	First XMM observation, 0.2–2 keV observed flux drop by a factor of ∼39 relative to eRASS5.
59 661	Detection of radio transient emission with ATCA in first radio follow-up observation.
59 693	First detection of outflow at 3000 km s^{-1} from Ly α absorption (FWHM∼14 000 km s^{-1}) in first *HST* spectrum (Engelthaler & Maksym 2023).

Table 8. Reported outflow properties of TDEs with X-ray observations pre-optical peak. Each of these objects have been followed up with different instruments and at different times, so there is not necessarily a common observed outflow indicator between systems. The expanding photosphere at early times points to a mechanical outflow only if it traces the motion of the debris (e.g. Nicholl et al. 2020).

Name	Outflow properties	Reference
AT2018dyb	H α blueshifted by $\sim$700 km s^{-1} in spectrum obtained $\sim$24 d before peak (although H α redshifted after optical peak).	Leloudas et al. (2019)
AT2019ahk	Photosphere expanding at $\sim$2700 km s^{-1} via modelling photometric rise, assuming constant temperature.	Holoien et al. (2019)
iPTF15af	No Hα detected in first optical spectrum near peak. Si IV blueshifted by $\sim$6000 km s^{-1} in *HST* spectrum obtained $\sim$28 d post-peak.	Blagorodnova et al. (2019)
AT2019azh	Transient radio emission detected $\sim$10 d before optical peak.	Goodwin et al. (2022a)
AT2019qiz	Photosphere expanding at $\sim$2200 km s^{-1} via modelling photometric rise, assuming constant temperature. Inferred outflow velocity $\lesssim$5000 km s^{-1} from asymmetric H α line in spectrum $\sim$9 d before peak.	Nicholl et al. (2020)
AT2020zso	Photosphere expanding at $\sim$2900 km s^{-1} via modelling photometric rise, assuming constant temperature.	Wevers et al. (2022)

Around 14 d before the optical peak, it is likely that we have an unobscured view onto the nascent disc, which is initially surrounded by an envelope of gas formed through shocks during the circularization process, as found in simulations (Bonnerot et al. 2021). While this envelope is initially of low enough density for the disc emission to promptly emerge, the envelope mass increases over time due to feeding by the outflowing gas in the system. As a result, the X-ray emission may be more efficiently absorbed over time, leading to the observed drop-off in the X-ray emission, and a reprocessed-driven optical brightening. To quantitatively test this scenario, we follow Roth et al. (2016) by modelling the envelope as a sphere of inner and outer radii $R_{\rm in}$ and $R_{\rm out}$, containing a mass of gas $M_{\rm env}$ distributed according to a density profile $\rho \propto R^{-2}$, which is irradiated by an inner source of luminosity L. The effective optical depth $\tau_{\rm eff}$ relevant for X-ray absorption is then given by their equation 27, relying on He II photoionization being the dominant absorption process and using solar composition. Here, we further assume that the envelope mass increases with time as $M_{\rm env} = \dot{M}_{\rm env} t$ due to feeding by early returning debris. The time at which the envelope is able to absorb the inner X-ray radiation is obtained by solving $\tau_{\rm eff}(t) = 1$, which gives

$$t_{\rm abs} = 24\,{\rm d} \left(\frac{L}{10^{43}\,{\rm erg\,s^{-1}}}\right)^{5/19} \left(\frac{\dot{M}_{\rm env}}{{\rm M_\odot\,yr^{-1}}}\right)^{-1} \left(\frac{R_{\rm in}}{10^{14}\,{\rm cm}}\right)^{20/19} \left(\frac{R_{\rm out}}{10^{15}\,{\rm cm}}\right)^{16/19}, \quad (1)$$

where the luminosity $L \approx 10^{43}$ erg s^{-1} is determined from that of the detected X-rays. This time is approximately consistent with the 19 d delay between the eRASS5 detection and first *XMM* observation, for an envelope feeding rate $\dot{M}_{\rm env} \approx {\rm M_\odot\,yr^{-1}}$, comparable to the debris fallback rate of a typical TDE near peak (e.g. Rossi et al. 2021). Within this interpretation, the early-time X-ray detection presented in this paper provides a new way to constrain physical properties such as the feeding rate and size of the envelope, and the luminosity of the obscured accretion disc, which are crucial to improve our theoretical understanding of these systems.

The origin of the early-time outflows seen in some TDEs is still unclear (see discussion in Goodwin et al. 2022a), but is thought to be due to either a stream-stream collision-induced outflow (CIO; e.g. Lu & Bonnerot 2020), debris unbounded by accretion luminosity (Metzger & Stone 2016) or a radiatively driven disc wind (Lodato & Rossi 2011; Miller 2015). The data set in this work does not allow us to distinguish between these mechanisms for AT 2022dsb, since each scenario would initially lead to an increased density of gas and optical depth along our line-of-sight as the fallback rate increases over time.[14]

Importantly, if the observed early-time evolution in AT 2022dsb is not unique to this system, then other TDEs may also be X-ray bright at early times, and become X-ray faint only when veiled by outflowing debris launched shortly after the onset of circularization.[15] Given that the existing models described above predict the launching of outflows which would extend large solid angles on the sky, as seen by the disrupting black hole, then a large fraction of optically bright TDEs may therefore be X-ray faint when followed up in the weeks-to-months after optical peak (unless viewed at angles peering through an optically thin funnel in the reprocessor; Metzger & Stone 2016; Dai et al. 2018; Lu & Bonnerot 2020).

7 SUMMARY

We reported on multiwavelength observations of the TDE candidate AT 2022dsb, whose main properties can be summarized as follows:

(i) eROSITA detected ultra-soft ($kT_{\rm BB} \sim 45$ eV) X-ray emission (0.2–2 keV $L_{\rm X} \sim 3 \times 10^{43}$ erg s^{-1}) from a TDE $\sim$14 d before optical peak. The eROSITA detection precedes the first 3σ detection in the optical, and occurs only $\sim$17 d after the inferred time of first mass fallback to pericentre.

(ii) An *XMM* follow-up observation 19 d after this eROSITA detection revealed a drop in the observed 0.2–2 keV flux by a factor of 39; during this period, the optical emission brightened to a maximum. A second *XMM* observation $\sim$173 d after the eROSITA detection showed a 0.2–2 keV flux and spectral properties consistent with this first *XMM* observation. No further X-ray emission was significantly detected above background by *Swift* XRT monitoring observations in the following $\sim$200 d after the eROSITA detection. Thus without the early-time eROSITA observation, AT 2022dsb would likely have been classified as an 'optically bright, X-ray quiet' TDE.

(iii) Follow-up optical spectra show a broad emission complex around the He II 4686 Å, broad H α emission and a strong blue continuum in the early-time spectra. The He II complex is clearly present in the spectra taken $\sim$5 d before optical peak, and is still detected $\sim$38 d after optical peak (even after the large amplitude X-ray dimming). The strength of these features with respect to the

[14] Future spectroscopic monitoring of TDEs in the UV may distinguish between these two origins.

[15] Alternatively, if the X-ray emission is above a critical luminosity, then all of the He II may be ionized to He III, enabling the X-ray emission to escape the system (Metzger & Stone 2016).

host galaxy emission decreases over the spectroscopic follow-up campaign.

(iv) Multiple outflow signatures are detected in the system at early times (transient radio emission with ATCA, first detected $\sim$20 d post-optical peak; blueshifted broad Hα emission at $\sim$1600 km s^{-1}, detected $\sim$5 d before optical peak, and blueshifted broad Lyα absorption at $\sim-$3000 km s^{-1}, detected $\sim$54 d after optical peak).

(v) The combination of these observed features suggests that outflows launched at early times may boost the density of the material enshrouding the nascent disc, leading to an increased amount of reprocessing of the high-energy disc emission. This causes an early drop-off in the observed X-ray flux whilst the optical brightens.

(vi) If the observed early-time properties are not unique to this system, then other TDEs may be X-ray bright at early times, and become X-ray faint when veiled by outflowing stellar debris. The X-ray vs optically bright nature of a TDE is also time dependent at early times.

The early-time X-ray emission from TDEs may be monitored in greater detail with the next-generation of time-domain missions, such as the *Einstein Probe* (*EP*; Yuan et al. 2018), launched in 2024 January, or through early follow-up of candidates identified with the *Ultraviolet Transient Astronomy Satellite* (*ULTRASAT*; Sagiv et al. 2014) and the Vera Rubin Observatory (Ivezić 2019). High-cadence X-ray monitoring observations of such early X-ray transients may provide a new way to constrain the mass feeding rate and nature of the reprocessing envelope in TDEs in future work.

ACKNOWLEDGEMENTS

AM is grateful to the generosity of Curtin University for hosting his visit, where parts of this work were completed. AM thanks the *XMM*, *Swift*, and *NICER* teams for approving the ToO requests. AM acknowledges support by DLR under the grant 50 QR 2110 (XMM_NuTra, PI: Z. Liu). This work was performed in part at the Aspen Center for Physics, which is supported by National Science Foundation grant PHY-2210452. We would like to thank the referee for a constructive report that improved the quality of the paper.

This work is based on data from eROSITA, the soft X-ray instrument aboard SRG, a joint Russian–German science mission supported by the Russian Space Agency (Roskosmos), in the interests of the Russian Academy of Sciences represented by its Space Research Institute (IKI), and the Deutsches Zentrum für Luft- und Raumfahrt (DLR). The SRG spacecraft was built by Lavochkin Association (NPOL) and its subcontractors, and is operated by NPOL with support from the Max Planck Institute for Extraterrestrial Physics (MPE).

The development and construction of the eROSITA X-ray instrument was led by MPE, with contributions from the Dr Karl Remeis Observatory Bamberg & ECAP (FAU Erlangen-Nuernberg), the University of Hamburg Observatory, the Leibniz Institute for Astrophysics Potsdam (AIP), and the Institute for Astronomy and Astrophysics of the University of Tübingen, with the support of DLR and the Max Planck Society. The Argelander Institute for Astronomy of the University of Bonn and the Ludwig Maximilians Universität Munich also participated in the science preparation for eROSITA.

The eROSITA data shown here were processed using the ESASS software system developed by the German eROSITA consortium.

The authors acknowledge support for obtaining the LCO/FLOYDS spectroscopy by the Deutsche Forschungsgemeinschaft (DFG, German Research Foundation) under Germany's Excellence Strategy – EXC-2094 - 390783311.

This work made use of data supplied by the UK Swift Science Data Centre at the University of Leicester.

The Australia Telescope Compact Array is part of the Australia Telescope National Facility[16] which is funded by the Australian Government for operation as a National Facility managed by CSIRO. We acknowledge the Gomeroi people as the Traditional Owners of the Observatory site.

The Legacy Surveys consist of three individual and complementary projects: the Dark Energy Camera Legacy Survey (DECaLS; Proposal ID 2014B-0404; PIs: David Schlegel and Arjun Dey), the Beijing–Arizona Sky Survey (BASS; NOAO Prop. ID 2015A-0801; PIs: Zhou Xu and Xiaohui Fan), and the Mayall z-band Legacy Survey (MzLS; Prop. ID 2016A-0453; PI: Arjun Dey). DECaLS, BASS, and MzLS together include data obtained, respectively, at the Blanco telescope, Cerro Tololo Inter-American Observatory, NSF's NOIRLab; the Bok telescope, Steward Observatory, University of Arizona; and the Mayall telescope, Kitt Peak National Observatory, NOIRLab. Pipeline processing and analyses of the data were supported by NOIRLab and the Lawrence Berkeley National Laboratory (LBNL). The Legacy Surveys project is honoured to be permitted to conduct astronomical research on Iolkam Du'ag (Kitt Peak), a mountain with particular significance to the Tohono O'odham Nation.

Some of the observations reported in this paper were obtained with the Southern African Large Telescope (SALT) under the programme 2021-2-LSP-001 (PI: DAHB). Polish participation in SALT is funded by grant no. MEiN nr2021/WK/01.

NOIRLab is operated by the Association of Universities for Research in Astronomy (AURA) under a cooperative agreement with the National Science Foundation. LBNL is managed by the Regents of the University of California under contract to the U.S. Department of Energy.

This project used data obtained with the Dark Energy Camera (DECam), which was constructed by the Dark Energy Survey (DES) collaboration. Funding for the DES Projects has been provided by the U.S. Department of Energy, the U.S. National Science Foundation, the Ministry of Science and Education of Spain, the Science and Technology Facilities Council of the United Kingdom, the Higher Education Funding Council for England, the National Center for Supercomputing Applications at the University of Illinois at Urbana–Champaign, the Kavli Institute of Cosmological Physics at the University of Chicago, Center for Cosmology, and Astro-Particle Physics at the Ohio State University, the Mitchell Institute for Fundamental Physics and Astronomy at Texas A&M University, Financiadora de Estudos e Projetos, Fundacao Carlos Chagas Filho de Amparo, Financiadora de Estudos e Projetos, Fundacao Carlos Chagas Filho de Amparo a Pesquisa do Estado do Rio de Janeiro, Conselho Nacional de Desenvolvimento Cientifico e Tecnologico and the Ministerio da Ciencia, Tecnologia e Inovacao, the Deutsche Forschungsgemeinschaft, and the Collaborating Institutions in the Dark Energy Survey. The Collaborating Institutions are Argonne National Laboratory, the University of California at Santa Cruz, the University of Cambridge, Centro de Investigaciones Energeticas, Medioambientales y Tecnologicas-Madrid, the University of Chicago, University College London, the DES-Brazil Consortium, the University of Edinburgh, the Eidgenossische Technische Hochschule (ETH) Zurich, Fermi National Accelerator Laboratory, the University of Illinois at Urbana–Champaign, the Institut de Ciencies de l'Espai (IEEC/CSIC), the Institut de Fisica d'Altes

[16] https://ror.org/05qajvd42

Energies, Lawrence Berkeley National Laboratory, the Ludwig Maximilians Universitat Munchen and the associated Excellence Cluster Universe, the University of Michigan, NSF's NOIRLab, the University of Nottingham, the Ohio State University, the University of Pennsylvania, the University of Portsmouth, SLAC National Accelerator Laboratory, Stanford University, the University of Sussex, and Texas A&M University.

BASS is a key project of the Telescope Access Program (TAP), which has been funded by the National Astronomical Observatories of China, the Chinese Academy of Sciences (the Strategic Priority Research Program 'The Emergence of Cosmological Structures' Grant XDB09000000), and the Special Fund for Astronomy from the Ministry of Finance. The BASS is also supported by the External Cooperation Program of Chinese Academy of Sciences (Grant 114A11KYSB20160057), and Chinese National Natural Science Foundation (Grant 12120101003, 11433005).

The Legacy Survey team makes use of data products from the Near-Earth Object Wide-field Infrared Survey Explorer (NEOWISE), which is a project of the Jet Propulsion Laboratory/California Institute of Technology. NEOWISE is funded by the National Aeronautics and Space Administration.

The Legacy Surveys imaging of the DESI footprint is supported by the Director, Office of Science, Office of High Energy Physics of the U.S. Department of Energy under Contract No. DE-AC02-05CH1123, by the National Energy Research Scientific Computing Center, a DOE Office of Science User Facility under the same contract; and by the U.S. National Science Foundation, Division of Astronomical Sciences under Contract No. AST-0950945 to NOAO.

This work has made use of data from the Asteroid Terrestrial-impact Last Alert System (ATLAS) project. The Asteroid Terrestrial-impact Last Alert System (ATLAS) project is primarily funded to search for near earth asteroids through NASA grants NN12AR55G, 80NSSC18K0284, and 80NSSC18K1575; byproducts of the NEO search include images and catalogues from the survey area. This work was partially funded by Kepler/K2 grant J1944/80NSSC19K0112 and HST GO-15889, and STFC grants ST/T000198/1 and ST/S006109/1. The ATLAS science products have been made possible through the contributions of the University of Hawaii Institute for Astronomy, the Queen's University Belfast, the Space Telescope Science Institute, the South African Astronomical Observatory, and The Millennium Institute of Astrophysics (MAS), Chile.

This work was supported by the Australian government through the Australian Research Council's Discovery Projects funding scheme (DP200102471).

DATA AVAILABILITY

The full eRASS1 data taken within the German half of the eROSITA sky was released to the public on Jannuary 31st 2024. eRASS2-5 data are expected to be released at a later stage. The *Swift* data is available to download through the UK Swift Data Science website.[17] The *XMM* data will become public after the propietory period expires (2023-09-21). Publicly available ATLAS data can be accessed through the ATLAS forced photometry service.[18] Publicly available ZTF data can be accessed through the ZTF forced photometry service.[19] NTT/EFOSC2 spectroscopy has been obtained under the program IDs 108.220C.012 (PI. C. Inserra) and 109.23JL.001 (PI. I. Grotova). All optical spectra are publicly available. ATCA data are stored in the Australia Telescope Online Archive,[20] and will become publicly accessible 18 months from the date of observation.

[17] https://www.swift.ac.uk/archive/index.php
[18] https://fallingstar-data.com/forcedphot/
[19] https://irsa.ipac.caltech.edu/Missions/ztf.html
[20] https://atoa.atnf.csiro.au/

REFERENCES

Alexander K. D., Berger E., Guillochon J., Zauderer B. A., Williams P. K. G., 2016, ApJ, 819, L25
Alexander K. D., Wieringa M. H., Berger E., Saxton R. D., Komossa S., 2017, ApJ, 837, 153
Anderson M. M. et al., 2020, ApJ, 903, 116
Arcavi I. et al., 2014, ApJ, 793, 38
Assef R. J., Stern D., Noirot G., Jun H. D., Cutri R. M., Eisenhardt P. R. M., 2018, ApJS, 234, 23
Bade N., Komossa S., Dahlem M., 1996, A&A, 309, L35
Bellm E. C. et al., 2019, PASP, 131, 018002
Blagorodnova N. et al., 2017, ApJ, 844, 46
Blagorodnova N. et al., 2019, ApJ, 873, 92
Bonnerot C., Lu W., Hopkins P. F., 2021, MNRAS, 504, 4885
Brown T. M. et al., 2013, PASP, 125, 1031
Brunner H. et al., 2022, A&A, 661, A1
Buchner J., 2021, J. Open Source Softw., 6, 3001
Buchner J. et al., 2014, A&A, 564, A125
Buckley D. A. H., Swart G. P., Meiring J. G., 2006, in Stepp L. M., ed., Proc. SPIE Conf. Ser. Vol. 6267, Ground-based and Airborne Telescopes. SPIE, Bellingham, p. 62670Z
Burgh E. B., Nordsieck K. H., Kobulnicky H. A., Williams T. B., O'Donoghue D., Smith M. P., Percival J. W., 2003, in Iye M., Moorwood A. F. M., eds, Proc. SPIE Conf. Ser. Vol. 4841, Instrument Design and Performance for Optical/Infrared Ground-based Telescopes. SPIE, Bellingham, p. 1463
Burrows D. N. et al., 2005, Space Sci. Rev., 120, 165
Cannizzaro G. et al., 2021, MNRAS, 504, 792
Cardelli J. A., Clayton G. C., Mathis J. S., 1989, ApJ, 345, 245
Carter B., Luminet J. P., 1983, A&A, 121, 97
Cash W., 1976, A&A, 52, 307
Cendes Y., Alexander K. D., Berger E., Eftekhari T., Williams P. K. G., Chornock R., 2021, ApJ, 919, 127
Cendes Y. et al., 2022, ApJ, 938, 28
Chabrier G., 2003, PASP, 115, 763
Chen Y.-P., Zaw I., Farrar G. R., Elgamal S., 2022, ApJS, 258, 29
Conroy C., Gunn J. E., 2010, Astrophysics Source Code Library, record ascl:1010.043
Crawford S. M. et al., 2010, in Silva D. R., Peck A. B., Soifer B. T., eds, SPIE Conf. Ser. Vol. 7737, Observatory Operations: Strategies, Processes, and Systems III. SPIE, Bellingham, p. 773725
Dai L., McKinney J. C., Roth N., Ramirez-Ruiz E., Miller M. C., 2018, ApJ, 859, L20
Dey A. et al., 2019, AJ, 157, 168
Engelthaler E., Maksym W., 2023, in American Astronomical Society Meeting Abstracts, 241, 301.14
Evans P. A. et al., 2007, A&A, 469, 379
Evans P. A. et al., 2009, MNRAS, 397, 1177
Flohic H. M. L. G., Eracleous M., Chartas G., Shields J. C., Moran E. C., 2006, ApJ, 647, 140
Foreman-Mackey D., Hogg D. W., Lang D., Goodman J., 2013, PASP, 125, 306
Foreman-Mackey D., Sick J., Johnson B., 2014, python-fsps: Python bindings to FSPS (v0.1.1), Zanodo, available at: https://zenodo.org/records/12157
Franchini A., Lodato G., Facchini S., 2016, MNRAS, 455, 1946
Fruscione A. et al., 2006, in Silva D. R., Doxsey R. E., eds, Proc. SPIE Conf. Ser. Vol.6270, Observatory Operations: Strategies, Processes, and Systems. SPIE, Bellingham, p. 586
Fulton M., Smith K. W., Moore T., Srivastav S., Bruch R. J., 2022, Transient Name Server Classification Report, 2022-584, 1

Förster F. et al., 2021, AJ, 161, 242
Gaia Collaboration, 2021, A&A, 649, A6
Gatuzz E., García J., Kallman T. R., Mendoza C., Gorczyca T. W., 2015, ApJ, 800, 29
Gehrels N. et al., 2004, in AIP Conf. Proc. Vol. 727, GAMMA-RAY BURSTS: 30 YEARS OF DISCOVERY: Gamma-Ray Burst Symposium. Am. Inst. Phys., New York, p. 637
Gezari S., 2021, ARA&A, 59, 21
Gezari S., Cenko S. B., Arcavi I., 2017, ApJ, 851, L47
González-Martín O., Masegosa J., Márquez I., Guainazzi M., Jiménez-Bailón E., 2009, A&A, 506, 1107
Goodwin A. J. et al., 2022a, MNRAS, 511, 5328
Goodwin A. J. et al., 2022b, MNRAS, 518, 847
Goodwin A. J. et al., 2023, MNRAS, 522, 5084
Graham M. J. et al., 2019, PASP, 131, 078001
Greiner J., Schwarz R., Zharikov S., Orio M., 2000, A&A, 362, L25
Grupe D., Thomas H. C., Leighly K. M., 1999, A&A, 350, L31
Gu M., Cao X., 2009, MNRAS, 399, 349
Guillochon J., Ramirez-Ruiz E., Rosswog S., Kasen D., 2009, ApJ, 705, 844
Guillochon J., Nicholl M., Villar V. A., Mockler B., Narayan G., Mandel K. S., Berger E., Williams P. K. G., 2018, ApJS, 236, 6
Guo H., Shen Y., Wang S., 2018, Astrophysics Source Code Library, record ascl:1809.008
Hammerstein E. et al., 2023, ApJ, 942, 9
Higson E., Handley W., Hobson M., Lasenby A., 2019, Stat. Comput., 29, 891
Hinkle J. T., Holoien T. W.-S., Shappee B. J., Auchettl K., 2021, ApJ, 910, 83
Holoien T. W.-S. et al., 2016, MNRAS, 455, 2918
Holoien T. W.-S. et al., 2019, ApJ, 883, 111
Homan D. et al., 2023, A&A, 672, A167
Horesh A., Cenko S. B., Arcavi I., 2021, Nat. Astron., 5, 491
Irwin J. A., Henriksen R. N., Krause M., Wang Q. D., Wiegert T., Murphy E. J., Heald G., Perlman E., 2018, ApJ, 860, 176
Ivezić Ž., 2019, ApJ, 873, 44
Johnson B. D., Leja J., Conroy C., Speagle J. S., 2021, ApJS, 254, 22
Jones D. H. et al., 2009, MNRAS, 399, 683
Kewley L. J., Dopita M. A., Sutherland R. S., Heisler C. A., Trevena J., 2001, ApJ, 556, 121
Komossa S., Bade N., 1999, A&A, 343, 775
Komossa S., Greiner J., 1999, A&A, 349, L45
Komossa S. et al., 2009, ApJ, 701, 105
Koposov S. et al., 2023, joshspeagle/dynesty: v2.1.0, Zenodo, available at: https://zenodo.org/records/8408702
Kraft R. P., Burrows D. N., Nousek J. A., 1991, ApJ, 374, 344
Lacy M. et al., 2020, PASP, 132, 035001
Leloudas G. et al., 2019, ApJ, 887, 218
Liu Z., Malyali A., Rau A., Merloni A., Krumpe M., 2022, Astron. Telegram, 15259, 1
Liu Z. et al., 2023, A&A, 669, A75
Lodato G., Rossi E. M., 2011, MNRAS, 410, 359
Loeb A., Ulmer A., 1997, ApJ, 489, 573
Lu W., Bonnerot C., 2020, MNRAS, 492, 686
Mainzer A. et al., 2014, ApJ, 792, 30
Malyali A. et al., 2021, A&A, 647, A9
Malyali A. et al., 2023a, MNRAS, 520, 3549
Malyali A. et al., 2023b, MNRAS, 520, 4209
Masci F. J. et al., 2019, PASP, 131, 018003
Metzger B. D., Stone N. C., 2016, MNRAS, 461, 948
Miller M. C., 2015, ApJ, 805, 83
Mockler B., Guillochon J., Ramirez-Ruiz E., 2019, ApJ, 872, 151
Nandra K., Pounds K. A., 1994, MNRAS, 268, 405
Narayan R., Mahadevan R., Quataert E., 1998, in Abramowicz M. A., Björnsson G., Pringle J. E., eds, Theory of Black Hole Accretion Disks. Cambridge Univ. Press, Cambridge, p. 148
Newville M., Stensitzki T., Allen D. B., Rawlik M., Ingargiola A., Nelson A. 2016, Astrophysics Source Code Library, record ascl:1606.014
Nicholl M., 2018, Research Notes of the AAS, 2, 230
Nicholl M. et al., 2020, MNRAS, 499, 482
Piran T., Svirski G., Krolik J., Cheng R. M., Shiokawa H., 2015, ApJ, 806, 164
Predehl P. et al., 2021, A&A, 647, A1
Rees M. J., 1988, Nature, 333, 523
Reines A. E., Volonteri M., 2015, ApJ, 813, 82
Roming P. W. A. et al., 2005, Space Sci. Rev., 120, 95
Rossi E. M., Stone N. C., Law-Smith J. A. P., Macleod M., Lodato G., Dai J. L., Mandel I., 2021, Space Sci. Rev., 217, 40
Roth N., Kasen D., Guillochon J., Ramirez-Ruiz E., 2016, ApJ, 827, 3
Sagiv I. et al., 2014, AJ, 147, 79
Saxton R., Komossa S., Auchettl K., Jonker P. G., 2020, Space Sci. Rev., 216, 85
Saxton R., Komossa S., Auchettl K., Jonker P. G., 2021, Space Sci. Rev., 217, 18
Sazonov S. et al., 2021, MNRAS, 508, 3820
Schlafly E. F., Finkbeiner D. P., 2011, ApJ, 737, 103
Shingles L. et al., 2021, Transient Name Server AstroNote, 7, 1
Shiokawa H., Krolik J. H., Cheng R. M., Piran T., Noble S. C., 2015, ApJ, 804, 85
Simmonds C., Buchner J., Salvato M., Hsu L.-T., Bauer F. E., 2018, A&A, 618, A66
Skilling J., 2004, in Fischer R., Preuss R., Toussaint U. V., eds, AIP Conf. Ser. Vol. 735, Bayesian Inference and Maximum Entropy Methods in Science and Engineering. Am. Inst. Phys., New York, p. 395
Skilling J., 2006, Bayesian Analysis, 1, 833
Smartt S. J. et al., 2015, A&A, 579, A40
Smith K. W. et al., 2020, PASP, 132, 085002
Speagle J. S., 2020, MNRAS, 493, 3132
Stanek K. Z., Kochanek C. S., 2022, Transient Name Server Discovery Report, 2022-559, 1
Stein R. et al., 2021, Nat. Astron., 5, 510
Stern D. et al., 2012, ApJ, 753, 30
Stone N., Loeb A., 2012, Phys. Rev. Lett., 108, 061302
Stone N., Sari R., Loeb A., 2013, MNRAS, 435, 1809
Sunyaev R. et al., 2021, A&A, 656, A132
The CASA Team et al., 2022, PASP, 134, 114501
Tody D., 1986, in Crawford D. L., ed., Proc. SPIE Conf. Ser Vol. 627, Instrumentation in Astronomy VI. SPIE, Bellingham, p. 733
Tonry J. L. et al., 2018, PASP, 130, 064505
Trümper J., 1982, Adv. Space Res., 2, 241
van Velzen S. et al., 2019, ApJ, 872, 198
van Velzen S., Holoien T. W.-S., Onori F., Hung T., Arcavi I., 2020, Space Sci. Rev., 216, 124
van Velzen S. et al., 2021, ApJ, 908, 4
Verner D. A., Ferland G. J., Korista K. T., Yakovlev D. G., 1996, ApJ, 465, 487
Wang T.-G., Zhou H.-Y., Wang L.-F., Lu H.-L., Xu D., 2011, ApJ, 740, 85
Wang T.-G., Zhou H.-Y., Komossa S., Wang H.-Y., Yuan W., Yang C., 2012, ApJ, 749, 115
Wevers T. et al., 2022, A&A, 666, A6
Willingale R., Starling R. L. C., Beardmore A. P., Tanvir N. R., O'Brien P. T., 2013, MNRAS, 431, 394
Wilms J., Allen A., McCray R., 2000, ApJ, 542, 914
Wright E. L. et al., 2010, AJ, 140, 1868
Yalinewich A., Guillochon J., Sari R., Loeb A., 2019, MNRAS, 482, 2872
Yuan W. et al., 2018, in den Herder J.-W. A., Nakazawa K., Nikzad S., eds, Proc. SPIE Conf. Ser. Vol. 10699, Space Telescopes and Instrumentation 2018: Ultraviolet to Gamma Ray. SPIE, Bellingham, p. 1069925

APPENDIX A: ADDITIONAL PHOTOMETRIC INFORMATION

The optical and UV photometry of AT 2022dsb is presented in Table A1.

Table A1. Optical and UV photometry of AT 2022dsb, corrected for Galactic extinction, and with 3σ upper limits presented.

MJD	Instrument	Filter	Magnitude
59 601.660	ATLAS	o	<19.21
59 610.660	ATLAS	o	<18.97
59 619.140	ATLAS	c	<18.14
59 624.095	ATLAS	o	<18.69
59 624.118	ATLAS	o	<19.59
59 627.077	ATLAS	o	<18.90
59 627.082	ATLAS	o	<18.90
59 627.086	ATLAS	o	<19.01
59 627.092	ATLAS	o	<18.97
59 628.113	ATLAS	o	<18.84
59 628.113	ATLAS	o	18.88 ± 0.34
59 628.127	ATLAS	o	<19.13
59 628.129	ATLAS	o	<18.97
59 628.129	ATLAS	o	18.64 ± 0.26
59 628.139	ATLAS	o	<18.58
59 628.140	ATLAS	o	<18.46
59 629.365	ATLAS	o	18.45 ± 0.13
59 630.344	ATLAS	o	18.19 ± 0.13
59 630.347	ATLAS	o	18.83 ± 0.20
59 630.364	ATLAS	o	17.73 ± 0.09
59 630.371	ATLAS	o	18.06 ± 0.12
59 637.330	ATLAS	o	17.77 ± 0.04
59 643.113	*Swift*	UVW1	16.24 ± 0.05
59 643.114	*Swift*	U	16.24 ± 0.06
59 643.114	*Swift*	B	15.68 ± 0.06
59 643.116	*Swift*	UVW2	15.52 ± 0.05
59 643.118	*Swift*	V	15.37 ± 0.07
59 643.120	*Swift*	UVM2	15.87 ± 0.05
59 644.110	ATLAS	o	18.12 ± 0.05
59 645.340	ATLAS	c	17.82 ± 0.06
59 647.070	ATLAS	o	17.77 ± 0.05
59 648.070	ATLAS	o	17.85 ± 0.03
59 649.769	*Swift*	UVW1	16.28 ± 0.06
59 649.771	*Swift*	U	16.16 ± 0.06
59 649.771	*Swift*	B	15.64 ± 0.06
59 649.773	*Swift*	UVW2	15.61 ± 0.05
59 649.774	*Swift*	V	15.34 ± 0.07
59 649.776	*Swift*	UVM2	15.91 ± 0.05
59 653.330	ATLAS	o	17.90 ± 0.04
59 654.350	ATLAS	o	18.27 ± 0.06
59 655.400	ATLAS	o	18.20 ± 0.08
59 656.020	ATLAS	o	18.26 ± 0.09
59 656.152	*Swift*	UVW1	16.94 ± 0.08
59 656.153	*Swift*	U	16.60 ± 0.09
59 656.154	*Swift*	B	16.04 ± 0.08
59 656.156	*Swift*	UVW2	16.54 ± 0.07
59 656.158	*Swift*	V	15.29 ± 0.08
59 656.160	*Swift*	UVM2	16.59 ± 0.08
59 657.330	ATLAS	o	18.29 ± 0.08
59 658.300	ATLAS	o	18.23 ± 0.09
59 662.600	ATLAS	o	18.74 ± 0.25
59 663.970	*Swift*	UVW1	17.26 ± 0.12
59 666.160	ATLAS	o	19.01 ± 0.12
59 668.126	*Swift*	UVW1	17.42 ± 0.09
59 668.127	*Swift*	U	16.98 ± 0.09
59 668.127	*Swift*	B	16.12 ± 0.07
59 668.128	*Swift*	UVW2	16.85 ± 0.07
59 668.129	*Swift*	V	15.58 ± 0.08
59 668.130	*Swift*	UVM2	17.09 ± 0.10
59 669.190	ATLAS	o	19.50 ± 0.15
59 670.310	ATLAS	o	19.94 ± 0.23
59 670.461	ZTF	r	19.10 ± 0.11
59 670.484	ZTF	g	19.07 ± 0.07
59 673.030	ATLAS	c	18.51 ± 0.10
59 673.417	ZTF	g	19.08 ± 0.11
59 673.481	ZTF	r	19.18 ± 0.17
59 673.807	*Swift*	UVW1	17.58 ± 0.11
59 673.809	*Swift*	U	16.99 ± 0.10
59 673.809	*Swift*	B	16.11 ± 0.08
59 673.811	*Swift*	UVW2	17.17 ± 0.12
59 674.260	ATLAS	o	19.33 ± 0.12
59 675.461	ZTF	g	19.15 ± 0.10
59 677.314	*Swift*	UVW1	17.84 ± 0.11
59 677.315	*Swift*	U	17.19 ± 0.10
59 677.316	*Swift*	B	16.15 ± 0.07
59 677.317	*Swift*	UVW2	17.26 ± 0.10
59 677.360	ATLAS	o	19.04 ± 0.22
59 677.462	ZTF	g	19.18 ± 0.14
59 678.280	ATLAS	o	19.13 ± 0.12
59 680.020	ATLAS	o	19.94 ± 0.17
59 682.270	ATLAS	o	<20.34
59 683.040	ATLAS	o	<17.64
59 683.207	*Swift*	UVW1	17.81 ± 0.16
59 683.208	*Swift*	U	17.34 ± 0.16
59 683.208	*Swift*	B	16.15 ± 0.10
59 683.210	*Swift*	UVW2	17.58 ± 0.15
59 683.211	*Swift*	V	15.59 ± 0.12
59 683.213	*Swift*	UVM2	17.47 ± 0.13
59 683.440	ZTF	g	19.55 ± 0.26
59 684.416	ZTF	r	<19.43
59 684.451	ZTF	g	19.38 ± 0.28
59 685.190	ATLAS	o	19.65 ± 0.34
59 689.418	ZTF	r	<19.06
59 689.461	ZTF	g	<19.06
59 690.320	ATLAS	o	19.38 ± 0.24
59 693.280	ATLAS	o	<20.41
59 694.330	ATLAS	o	<20.21
59 694.377	ZTF	g	<20.38
59 696.337	ZTF	g	19.92 ± 0.21
59 696.447	ZTF	r	20.04 ± 0.30
59 696.480	*Swift*	UVM2	17.74 ± 0.16
59 696.482	*Swift*	UVW1	18.24 ± 0.17
59 696.482	*Swift*	U	17.34 ± 0.11
59 696.483	*Swift*	UVW2	18.15 ± 0.18
59 697.300	ATLAS	o	19.55 ± 0.14
59 698.270	ATLAS	o	19.62 ± 0.17
59 699.020	ATLAS	o	20.06 ± 0.22
59 699.355	ZTF	r	<20.37
59699.440	ZTF	g	19.80 ± 0.17
59 700.070	ATLAS	o	<20.69
59 701.270	ATLAS	o	<18.80
59 701.376	ZTF	g	20.46 ± 0.31
59 701.418	ZTF	g	19.89 ± 0.17
59 701.424	*Swift*	UVM2	18.61 ± 0.27
59 701.425	*Swift*	UVW1	18.17 ± 0.16
59 701.426	*Swift*	U	17.41 ± 0.11
59 701.427	*Swift*	UVW2	17.76 ± 0.13
59 702.290	ATLAS	o	<20.37
59 703.470	ATLAS	o	<20.87
59 704.748	*Swift*	UVM2	17.90 ± 0.14
59 704.750	*Swift*	UVW1	18.16 ± 0.13
59 704.752	*Swift*	U	17.48 ± 0.09
59 704.753	*Swift*	UVW2	18.19 ± 0.15
59 705.310	ATLAS	o	<18.27
59 706.240	ATLAS	o	<20.64
59 707.397	ZTF	r	<20.14

Table A1 – *continued*

MJD	Instrument	Filter	Magnitude
59 709.230	ATLAS	o	19.69 ± 0.21
59 709.378	ZTF	r	<20.13
59 710.310	ATLAS	o	<17.74
59 712.540	ATLAS	o	<18.81
59 723.990	ATLAS	o	19.78 ± 0.25
59 725.200	ATLAS	o	19.66 ± 0.12
59 726.590	ATLAS	o	19.85 ± 0.15
59 729.054	*Swift*	U	17.24 ± 0.16
59 729.055	*Swift*	UVW2	18.19 ± 0.24
59 729.577	*Swift*	UVW1	18.15 ± 0.21
59 729.978	*Swift*	UVM2	18.38 ± 0.20
59 730.920	ATLAS	o	<20.52
59 731.960	ATLAS	o	20.09 ± 0.24
59 734.960	ATLAS	o	20.40 ± 0.36
59 735.804	*Swift*	UVM2	18.46 ± 0.22
59 735.808	*Swift*	UVW1	18.52 ± 0.17
59 735.810	*Swift*	U	17.47 ± 0.10
59 735.814	*Swift*	UVW2	18.37 ± 0.15
59 735.910	ATLAS	o	19.72 ± 0.14
59 737.180	ATLAS	o	<20.72
59 745.310	ATLAS	o	<18.20
59 749.140	ATLAS	o	<20.22
59 750.190	ATLAS	o	<19.89
59 765.100	ATLAS	o	<19.91
59 766.790	ATLAS	o	<20.59
59 767.820	ATLAS	o	<20.07
59 773.150	ATLAS	o	19.15 ± 0.34
59 775.840	ATLAS	o	<20.29
59 781.070	ATLAS	o	19.45 ± 0.18
59 782.100	ATLAS	o	<20.57
59 783.840	ATLAS	c	<20.43
59 785.100	ATLAS	o	<20.55
59 786.060	ATLAS	o	<20.03
59 787.860	ATLAS	c	20.58 ± 0.36
59 789.060	ATLAS	c	20.40 ± 0.28
59 790.410	ATLAS	c	20.53 ± 0.29
59 791.780	ATLAS	c	<20.71
59 793.080	ATLAS	c	20.31 ± 0.27
59 795.830	ATLAS	o	<19.88
59 799.810	ATLAS	o	<16.37
59 801.080	ATLAS	o	<19.45
59 802.070	ATLAS	o	<17.68
59 805.020	ATLAS	o	<20.24
59 806.450	ATLAS	o	<20.44
59 807.750	ATLAS	o	<20.52
59 814.790	ATLAS	o	<20.43
59 815.740	ATLAS	o	19.70 ± 0.35
59 817.520	ATLAS	c	19.96 ± 0.15
59 818.010	ATLAS	c	<19.87
59 818.750	ATLAS	o	<20.19
59 820.990	ATLAS	c	19.22 ± 0.17
59 821.010	ATLAS	c	20.30 ± 0.32
59 822.050	ATLAS	c	20.03 ± 0.25
59 822.790	ATLAS	o	<18.97
59 825.980	ATLAS	o	<19.02
59 828.990	ATLAS	o	<19.25
59 830.770	ATLAS	o	<19.78
59 855.514	*Swift*	UVW2	18.53 ± 0.15
59 855.518	*Swift*	UVM2	18.52 ± 0.17
59 855.524	*Swift*	UVW1	18.61 ± 0.13

APPENDIX B: ADDITIONAL SPECTROSCOPIC INFORMATION

A zoom-in on the evolution of the broad He II and Hα line profiles is presented in Fig. B1, whilst details on the spectroscopic observations and data reduction are presented below (see Table B1 for an observation log). The archival 6dFGS optical spectrum taken in 2002 is plotted in Fig. B2.

FLOYDS: AT 2022dsb was observed five times with the FLOYDS spectrographs mounted at the Las Cumbres Observatory 2 m telescopes at Siding Springs Observatory (FTS, Australia) and Haleakala

Table B1. Spectroscopic observations of AT 2022dsb.

MJD	UT	Telescope	Instrument	Airmass	Exposure [s]
59 636	2022-02-26	LCO FTN	FLOYDS	1.4	2400
59 640	2022-03-02	NTT	EFOSC2	1.0	600
59 665	2022-03-27	SALT	RSS	1.3	500
59 680	2022-04-11	SALT	RSS	1.2	500
59 680	2022-04-11	LCO FTS	FLOYDS	1.1	2400
59 699	2022-04-30	LCO FTS	FLOYDS	1.2	2400
59 726	2022-05-27	LCO FTN	FLOYDS	1.5	2400
59 767	2022-07-07	NTT	EFOSC2	1.2	1800
59 781	2022-07-21	LCO FTS	FLOYDS	1.4	2400

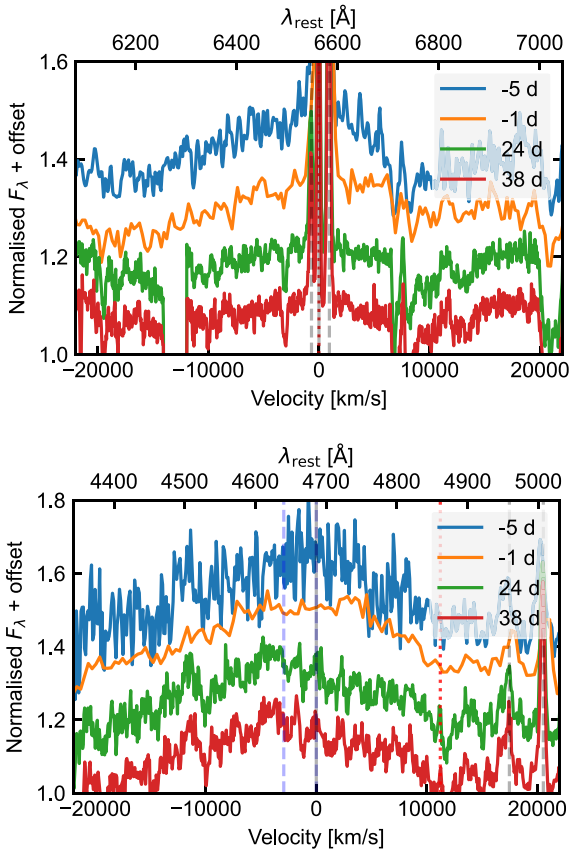

Figure B1. Evolution of the H α (top) and He II (bottom) line regions for the first four spectra that clearly show broad emission lines. The vertical lines mark [N II] 6548 Å, H α, and [N II] 6583 Å in the top panel (left to right), and N III 4640 Å, He II 4686 Å, H β, [O III] 4959 Å, and [O III] 5007 Å in the bottom panel.

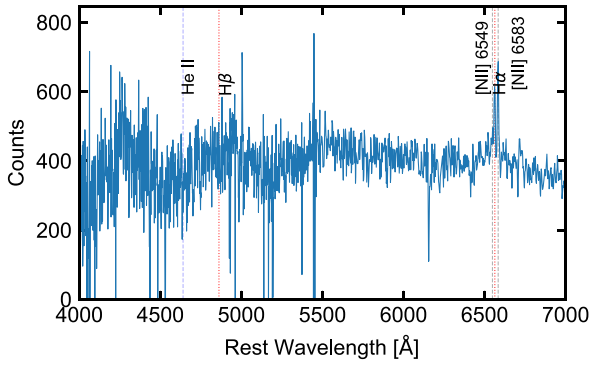

Figure B2. Archival optical spectrum of the host galaxy of AT 2022dsb taken in 2002 by 6dFGS (Jones et al. 2009). The broad He II emission complex around 4640 Å seen in the optical specroscopic follow-up campaign of AT 2022dsb is clearly not detected. The publicly available 6dFGS spectra do not have absolute flux calibrations.

(FTN, Hawaii). Observations were performed on 2022-2-26 (FTN), 2022-4-11 and 2022-4-30 (both FTS), 2022-5-27 (FTN), and 2022-7-21 (FTS) with 2400 s exposure each. The two identical FLOYDS are cross-dispersed low-resolution spectrographs covering the wavelength range from 320 to 1000 nm with a resolution between R = 400 and R = 700. Data were automatically processed by the standard FLOYDS pipeline.

SALT: Spectroscopy of AT 2022dsb was undertaken with the Southern African Large Telescope (SALT; Buckley, Swart & Meiring 2006) using the Robert Stobie Spectrograph (RSS; Burgh et al. 2003), on two nights: 2022 March 27 and 2022 April 11, starting 23:02 and 03:28 UTC, respectively. Two consecutive 500 sec exposure spectra with the PG0900 grating were obtained on each night. The spectra covered the region 4345–7400 Å at a mean resolution of 5.7 Å. The spectra were reduced using the PyRAF-based PySALT package (Crawford et al. 2010),[21] which includes corrections for gain and cross-talk, and performs bias subtraction. We extracted the science spectrum using standard IRAF[22] tasks, including wavelength calibration (Xenon calibration lamp exposures were taken, immediately after the science spectra), background subtraction, and 1D spectra extraction. Due to SALT's optical design, absolute flux calibration is not possible.[23] Observations of spectrophotometric standards during twilight were used to obtain relative flux calibration.

EFOSC2: The source was reobserved with the EFOSC2 spectrograph mounted at the ESO New Technology Telescope (NTT) at La Silla observatory on 2022-7-7 as part of a programme targeting eROSITA-selected TDEs (PI: Grotova; 109.23JL.001). Observations were performed with Grism#13 covering approx. 3600–9300 Å with a resolution of ≈21 Å, and an exposure time of 1800 s. The data were standard reduced with the IRAF (Tody 1986) community distribution.[24] The EFOSC2 spectrum taken on 2022-03-02 also used Grism#13, and was reduced by the ePESSTO + team (Smartt et al. 2015) using version `ntt_2.4.0` of their NTT reduction pipeline;[25] the reduced spectrum was downloaded from the Weizmann Interactive Supernova Data Repository (WISeREP[26]).

[21] https://astronomers.salt.ac.za/software/
[22] https://iraf-community.github.io/
[23] The entrance pupil changes its position during an observation, resulting in a changing effective collecting area.
[24] https://iraf-community.github.io
[25] https://github.com/svalenti/pessto
[26] https://www.wiserep.org/

This paper has been typeset from a TEX/LATEX file prepared by the author.